Dynamics of a charged Ziegler’s double pendulum with a nonholonomic constraint under the joint action of a dead force and a Lorentz force

Dynamics of a charged Ziegler's double pendulum with a nonholonomic constraint under the joint action of a dead force and a Lorentz force

Andrea Pastore[a], Joel C. Harrop[b], Davide Bigoni[b], Alfio Grillo[1a]

[a]*Dipartimento di Scienze Matematiche (DISMA) 'G.L. Lagrange', Politecnico di Torino, Corso Duca degli Abruzzi 24, Torino, 10129, Italy*
[b]*Instabilities Lab, University of Trento, Via Mesiano 77, Trento, 38123, Italy*

Abstract

A variant of viscoelastic Ziegler's double pendulum is investigated in which an electric charge is concentrated at one end of the device, at which a structural element imposing a nonholonomic constraint is attached. The obtained device is called 'charged Ziegler's double pendulum' and is subjected to the influence of a dead force and a Lorentz force. The latter results from an electric field and a magnetic induction field generated by an ideal solenoid. The mechanical system models a self-propelled microrobot and, in the absence of damping, is conservative up to the energy variation induced by the Lorentz force in the case of explicitly time dependent electric field. Within this framework, two situations are analyzed: Case I, in which the device is placed inside the solenoid and experiences a Lorentz force featuring both electric and magnetic part; Case II, in which the device is placed outside the solenoid and undergoes a Lorentz force due to the sole electric field. After determining the equilibrium for the system under study, a stability analysis is performed, and the conditions are obtained for flutter instability and Hopf bifurcation. In addition, the post-critical behavior of the structure is examined, focusing on the interaction between the Lorentz force and the other forces characterizing its dynamics. We investigate the possibility of revisiting, in the mechanical context provided by Ziegler's double pendulum, a phenomenology known in electromagnetism as Maxwell–Lodge effect.

Keywords: Ziegler's double pendulum, Nonholonomic constraints, Flutter instability, Hopf bifurcation, Ideal solenoid, Lorentz force, Maxwell–Lodge effect, Microrobotics
PACS: 03.50.De, 05.45.-a, 45.05.+x, 45.20.Jj, 45.40.Ln, 87.85.gj, 87.85.St
2000 MSC: 00A69, 37G15, 37J20, 37J60, 70E50, 70F25, 74F15

Acknowledgements

A.P and A.G. has been partially funded by the research project 'Innovative multiscale approaches, possibly based on Fractional Calculus, for the effective constitutive modeling of cell mechanics, engineered tissues, and metamaterials in Biomedicine and related fields', PRIN PNRR P2022KHFNB. D.B. and J.H. acknowledge financial support from the European Research Council (ERC) under the European Union's Horizon Europe research and innovation programme (Grant agreement No. ERC-ADG-2021-101052956-BEYOND). The methodologies developed in this work fall within the aims of the GNFM (Gruppo Nazionale per la Fisica Matematica) of the INDAM (Istituto Nazionale di Alta Matematica).

[1]Corresponding author: alfio.grillo@polito.it

Graphical Abstract

Dynamics of a charged Ziegler's double pendulum with a nonholonomic constraint under the joint action of a dead force and a Lorentz force

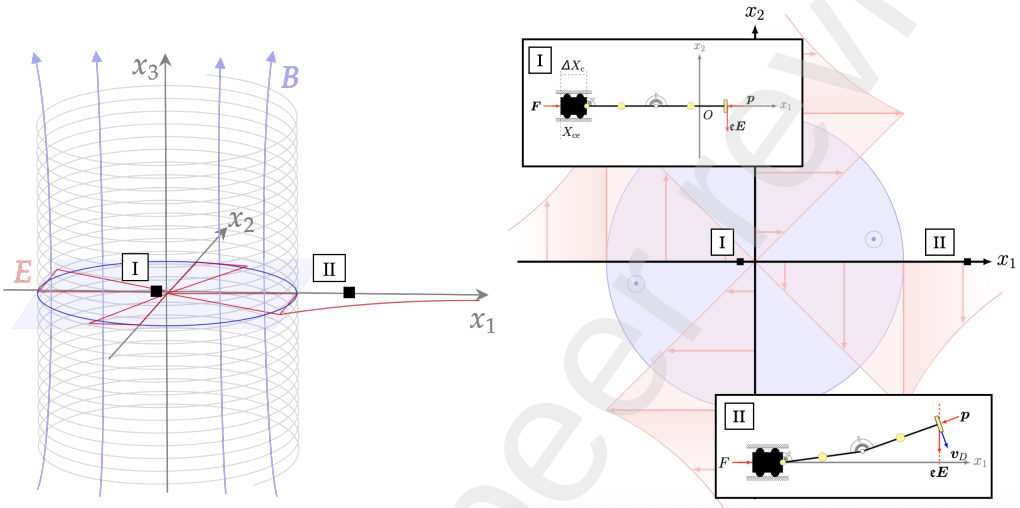

Highlights

Dynamics of a charged Ziegler's double pendulum with a nonholonomic constraint under the joint action of a dead force and a Lorentz force

- The interplay between a follower force and the Lorentz force
- The dynamics of a charged microrobot is triggered by the Lorentz force generated by the electromagnetic field inside an ideal solenoid and in the nearby outer space through a time-dependent vector potential
- The appearance of the Lorentz force in the outer space seems to be a manifestation of the Maxwell–Lodge effect

Dynamics of a charged Ziegler's double pendulum with a nonholonomic constraint under the joint action of a dead force and a Lorentz force

Abstract

A variant of viscoelastic Ziegler's double pendulum is investigated in which an electric charge is concentrated at one end of the device, at which a structural element imposing a nonholonomic constraint is attached. The obtained device is called 'charged Ziegler's double pendulum' and is subjected to the influence of a dead force and a Lorentz force. The latter results from an electric field and a magnetic induction field generated by an ideal solenoid. The mechanical system models a self-propelled microrobot and, in the absence of damping, is conservative up to the energy variation induced by the Lorentz force in the case of explicitly time dependent electric field. Within this framework, two situations are analyzed: Case I, in which the device is placed inside the solenoid and experiences a Lorentz force featuring both electric and magnetic part; Case II, in which the device is placed outside the solenoid and undergoes a Lorentz force due to the sole electric field. After determining the equilibrium for the system under study, a stability analysis is performed, and the conditions are obtained for flutter instability and Hopf bifurcation. In addition, the post-critical behavior of the structure is examined, focusing on the interaction between the Lorentz force and the other forces characterizing its dynamics. We investigate the possibility of revisiting, in the mechanical context provided by Ziegler's double pendulum, a phenomenology known in electromagnetism as Maxwell–Lodge effect.

Keywords: Ziegler's double pendulum, Nonholonomic constraints, Flutter instability, Hopf bifurcation, Ideal solenoid, Lorentz force, Maxwell–Lodge effect, Microrobotics
PACS: 03.50.De, 05.45.-a, 45.05.+x, 45.20.Jj, 45.40.Ln, 87.85.gj, 87.85.St
2000 MSC: 00A69, 37G15, 37J20, 37J60, 70E50, 70F25, 74F15

1. Introduction

The double pendulum is a mechanical device that, because of its simplicity, is often employed to exemplify more complicated structures, which appear in various mechanical contexts, ranging from different branches of engineering [1, 2] to robotics [3, 4], and biomechanics [5].

One variant of the double pendulum is Ziegler's double pendulum [6], constructed by two homogeneous and rigid bars, of equal length ℓ and equal mass m, connected one to the other via a hinge. The masses of the bars are considered to be concentrated at their midpoints. One of the two bars is hinged on a fixed frame, and the other is subjected to a force directed in parallel to it, known as a follower force. Moreover, the hinges are regarded as viscoelastic, with angular stiffness $k > 0$, and damping $c > 0$. These coefficients lump the viscoelastic properties of the structure into the joints connecting the double pendulum to the fixed frame and the two bars to

each other [6, 7]. An important feature of Ziegler's double pendulum is that it can exhibit flutter instability due to the non-conservative nature of the follower force [1, 6, 8, 9, 10].

Cazzolli et al. [3] introduced a modification of Ziegler's double pendulum that reproduces the same bifurcation and instability landscape as the original structure, but *under a conservative load*. In particular, one end of the first bar is pinned to a moving cart (Figure 1); at the tip of the second bar, a nonholonomic constraint enforces orthogonality between the tip velocity and the bar. This system is designed in a way that it can allow a translational motion of the cart, when the latter is loaded with a dead force, possible through an oscillatory motion of the arms of the pendulum, a dynamics resembling those of a certain family of microrobots or micro-structures used in biomechanics [5, 11, 12, 13, 14]. One example of these microrobots is provided by a *'magnetic flexible filament attached to a red blood cell'*, as presented by Dreyfus et al. [15], where the dead load plays the role of the propulsion thrust in aqueous environment at low Reynolds numbers. This device prompted the present investigation of analogous systems in microrobotics through a generalization of the loads considered in [3].

Microrobots for biomedical or biomechanical applications are often susceptible to electro-magnetic interactions, because they feature magnetized [13, 14, 15] or electrically polarized parts [16]. Therefore, also Lorentz-type forces contribute to determine the overall dynamics of such devices in addition to self-propulsion [12] or other stimuli [5].

Despite its fundamental role in physics, certain foundational aspects of electromagnetism have remained the subject of debate until recently. This applies, for instance, to the true role and *'physical meaning'* [17] within classical electromagnetism of the vector potential $\boldsymbol{A}$, by which the magnetic induction field $\boldsymbol{B}$ is expressed as $\boldsymbol{B} = \mathrm{curl}\boldsymbol{A}$. Indeed, whereas the electric and the magnetic fields both have 'tangible' meaning, the vector potential works 'behind the scenes' of the classical theory of electromagnetism. This issue has been thoroughly investigated in a work by Rousseaux et al. [17], who conclude that there exist effects which cannot be understood *'without the intervention of'* $\boldsymbol{A}$ [17]. As an example for pursuing their goals, Rousseaux et al. [17] took the paradigmatic problem of the ideal solenoid to unveil the Maxwell–Lodge effect [18]. This phenomenon predicts that a current is generated in a wire wound around the solenoid in response to the electric field induced outside it by the variation in time of the vector potential (not of the magnetic induction field, which is zero outside the ideal solenoid). Although the purpose of this work is not to address the intricacies of the debate surrounding the vector potential, we embrace the viewpoint of Rousseaux et al. [17] and apply it to our mechanical device.

In light of the above considerations, the device investigated here can be regarded as a model of an electrically charged microrobot, with dimensions comparable to those of eukaryotic cells. It consists of a continuous viscoelastic rod attached to a small mass and is subjected to the Lorentz force generated by a solenoid [5, 11, 12, 13, 14]. The rod is idealized as a viscoelastic double pendulum, following the approach of Cazzolli et al. [3]. Compared to that approach, two substantial differences are introduced: (i) the dead load is interpreted as a self-propulsion force; (ii) the device carries a concentrated electric charge located in the structural element imposing the nonholonomic constraint (similar problems were formulated by Maruskin et al. [19] and Pastore et al. [20]).

Within this setting, the main objectives of our work are twofold:

1. We aim to assess the extent to which the Lorentz force modifies the results reported by Cazzolli et al. [3] concerning stability, the onset of a Hopf bifurcation, and the overall dynamical behavior of the device.
2. We revisit the Maxwell–Lodge effect [17] by placing it in the mechanical context of the

device under study. More specifically, we show that our theoretical framework predicts a Lorentz force on the charged structural element, even when it is located outside the solenoid. This result is achieved by placing the device first inside and then outside the solenoid. This may provide a potential–albeit presently theoretical–experimental setup to detect the Maxwell–Lodge effect, based on microrobotics and serving as an alternative to the experiment by Rousseaux et al. [17].

Outline of the work. The features of the device introduced by Cazzolli et al. [3] are outlined in Section 2, while in Section 3 the main electromagnetic aspects of our work are addressed (Section 3.1), including the way in which they affect the Lagrangian formalism of Ziegler's double-pendulum (Section 3.2). Section 3.3 presents the governing dynamic equations, incorporating the Lorentz force, while Section 3.4 addresses the corresponding static equilibrium. Based on the determination of the static equilibrium, a stability analysis is carried out for neighboring configurations (Section 4). Specifically, after linearizing the dynamic equations around equilibrium and studying the nature of the roots of the associated characteristic polynomial (Section 4.1), the presence of a Hopf bifurcation is shown (Section 4.2). Finally, Section 5 presents numerical simulations of two virtual experimental tests in the context of microrobotics.

2. Basic problem description, Lagrangian function and the 'skate' constraint

The version of Ziegler's double pendulum introduced by Cazzolli et al. [3] and used in the present investigation consists of two homogeneous and rigid bars, denoted by $\mathscr{B}_1$ and $\mathscr{B}_2$, each of length ℓ and mass m, connected by a hinge that links the right end of $\mathscr{B}_1$ to left end of $\mathscr{B}_2$. The left end of the bar $\mathscr{B}_1$ is hinged on a cart, which is free to move along a straight line on a fixed plane. A wheel is mounted at the right end of bar $\mathscr{B}_2$, the bar acting as its axle, and rolls without slipping on a fixed plane. The non-slipping wheel is the realization of a nonholonomic constraint of the 'skate' type. Overall, the device may experience only planar motions, parallel to the fixed plane, Figure 1.

In a fixed Cartesian reference frame with origin O and axes aligned with the orthonormal vectors $\boldsymbol{e}_1$, $\boldsymbol{e}_2$, and $\boldsymbol{e}_3$, the motion of the device is confined to the plane spanned by $\boldsymbol{e}_1$ and $\boldsymbol{e}_2$. Angles θ_1 and θ_2 measure the time-dependent inclinations of the bars $\mathscr{B}_1$ and $\mathscr{B}_2$ with the axis parallel to $\boldsymbol{e}_1$, respectively. Moreover, X_c denotes the instantaneous position, measured from O along $\boldsymbol{e}_1$, of the point of the cart to which $\mathscr{B}_1$ is hinged, Figure 1. The Lagrangian parameters θ_1, θ_2, and X_c, together with their velocities and accelerations, are collected in the arrays $q := (\theta_1, \theta_2, X_\mathrm{c})$, $\dot{q} := (\dot{\theta}_1, \dot{\theta}_2, \dot{X}_\mathrm{c})$, and $\ddot{q} := (\ddot{\theta}_1, \ddot{\theta}_2, \ddot{X}_\mathrm{c})$. Moreover, we introduce the following points of interest, whose spatial positions are expressed as functions of the Lagrangian coordinates:

$$x_A = \hat{x}_A(q) = (X_\mathrm{c}, 0, 0), \tag{1a}$$

$$x_B = \hat{x}_B(q) = (X_\mathrm{c} + \tfrac{1}{2}\ell\cos\theta_1, \tfrac{1}{2}\ell\sin\theta_1, 0), \tag{1b}$$

$$x_M = \hat{x}_M(q) = (X_\mathrm{c} + \ell\cos\theta_1, \ell\sin\theta_1, 0), \tag{1c}$$

$$x_C = \hat{x}_C(q) = (X_\mathrm{c} + \ell\cos\theta_1 + \tfrac{1}{2}\ell\cos\theta_2, \ell\sin\theta_1 + \tfrac{1}{2}\ell\sin\theta_2, 0), \tag{1d}$$

$$x_D = \hat{x}_D(q) = (X_\mathrm{c} + \ell\cos\theta_1 + \ell\cos\theta_2, \ell\sin\theta_1 + \ell\sin\theta_2, 0), \tag{1e}$$

which represent, in order: the position of the cart (point A); the midpoint of $\mathscr{B}_1$ (point B); the hinge connecting $\mathscr{B}_1$ to $\mathscr{B}_2$ (point M); the midpoint of $\mathscr{B}_2$ (point C); and the position of the

massless wheel (point D). Accordingly, the instantaneous orientations of the bars $\mathscr{B}_1$ and $\mathscr{B}_2$ are given by the unit vectors

$$\boldsymbol{n}_1 \equiv \hat{\boldsymbol{n}}_1(q) = (\cos\theta_1)\boldsymbol{e}_1 + (\sin\theta_1)\boldsymbol{e}_2, \qquad \boldsymbol{n}_2 \equiv \hat{\boldsymbol{n}}_2(q) = (\cos\theta_2)\boldsymbol{e}_1 + (\sin\theta_2)\boldsymbol{e}_2, \tag{2}$$

while the velocities of the points of interest are

$$\boldsymbol{v}_A = \hat{\boldsymbol{v}}_A(q,\dot{q}) = \dot{X}_\mathrm{c}\,\boldsymbol{e}_1, \tag{3a}$$

$$\boldsymbol{v}_B = \hat{\boldsymbol{v}}_B(q,\dot{q}) = [\dot{X}_\mathrm{c} - \tfrac{1}{2}\ell\,\dot{\theta}_1\sin\theta_1]\,\boldsymbol{e}_1 + [\tfrac{1}{2}\ell\dot{\theta}_1\cos\theta_1]\,\boldsymbol{e}_2, \tag{3b}$$

$$\boldsymbol{v}_M = \hat{\boldsymbol{v}}_M(q,\dot{q}) = [\dot{X}_\mathrm{c} - \ell\,\dot{\theta}_1\sin\theta_1]\,\boldsymbol{e}_1 + [\ell\,\dot{\theta}_1\cos\theta_1]\,\boldsymbol{e}_2, \tag{3c}$$

$$\boldsymbol{v}_C = \hat{\boldsymbol{v}}_C(q,\dot{q}) = [\dot{X}_\mathrm{c} - \ell\,\dot{\theta}_1\sin\theta_1 - \tfrac{1}{2}\ell\,\dot{\theta}_2\sin\theta_2]\,\boldsymbol{e}_1 + [\ell\dot{\theta}_1\cos\theta_1 + \tfrac{1}{2}\ell\,\dot{\theta}_2\cos\theta_2]\,\boldsymbol{e}_2, \tag{3d}$$

$$\boldsymbol{v}_D = \hat{\boldsymbol{v}}_D(q,\dot{q}) = [\dot{X}_\mathrm{c} - \ell\,\dot{\theta}_1\sin\theta_1 - \ell\,\dot{\theta}_2\sin\theta_2]\,\boldsymbol{e}_1 + [\ell\,\dot{\theta}_1\cos\theta_1 + \ell\,\dot{\theta}_2\cos\theta_2]\,\boldsymbol{e}_2. \tag{3e}$$

The presence of the wheel and the postulate on its motion impose a *nonholonomic constraint*: the velocity $\boldsymbol{v}_D$ of the end-point of $\mathscr{B}_2$ connected to the wheel is compelled to be at all times orthogonal to $\mathscr{B}_2$ (see [3] for details). In the considered reference frame, this constraint is described by the relation $\boldsymbol{n}_2 \cdot \boldsymbol{v}_D = 0$, which, in terms of the Lagrangian parameters and up to the sign, reads

$$C \equiv \hat{C}(q,\dot{q}) = \dot{\theta}_1\ell\sin(\theta_1-\theta_2) - \dot{X}_\mathrm{c}\cos\theta_2 = 0, \tag{4}$$

and is referred to as *"skate' constraint'* [3].

To simplify the analysis of the dynamics of the considered device, we prescribe that the mass of each bar is concentrated at its midpoint, that the cart can be modeled as a material point of mass m_c, and that the wheel's mass is negligible (*'massless wheel'* [3]). Moreover, we assume that the cart and $\mathscr{B}_1$ as well as $\mathscr{B}_1$ and $\mathscr{B}_2$ are connected to each other by means of viscoelastic spring-like elements of angular stiffness $k > 0$ and damping coefficient $c > 0$. Finally, a constant force $\boldsymbol{F} = F\boldsymbol{e}_1$ of magnitude $F > 0$ (*'dead load'* [3]) is applied to the cart, while a *'follower force'* [3], generated by the nonholonomic constraint, acts on the skate parallel to the bar $\mathscr{B}_2$, as shown in Figure 1.

Under the assumptions above, the system admits the Lagrangian function [3]

$$\begin{aligned}\mathcal{L}_\mathrm{o} \equiv \hat{\mathcal{L}}_\mathrm{o}(q,\dot{q}) =& \tfrac{1}{2}[\tfrac{5}{4}m\ell^2\dot{\theta}_1^2 + \tfrac{1}{4}m\ell^2\dot{\theta}_2^2 + (2m+m_\mathrm{c})\dot{X}_\mathrm{c}^2] \\ &+ \tfrac{1}{2}m\ell^2\,\dot{\theta}_1\dot{\theta}_2\cos(\theta_2-\theta_1) - \tfrac{3}{2}m\ell\,\dot{\theta}_1\dot{X}_\mathrm{c}\sin\theta_1 - \tfrac{1}{2}m\ell\,\dot{\theta}_2\dot{X}_\mathrm{c}\sin\theta_2 \\ &- \tfrac{1}{2}k\,\theta_1^2 - \tfrac{1}{2}k(\theta_2-\theta_1)^2 + F\,X_\mathrm{c},\end{aligned} \tag{5}$$

which accounts for all interactions to which the system is subjected, with the exception of the damping and of the nonholonomic constraint (4). Following [3], damping is described through the Rayleigh dissipation function

$$\mathcal{R} = \hat{\mathcal{R}}(\dot{q}) = \tfrac{1}{2}c\,\dot{\theta}_1^2 + \tfrac{1}{2}c(\dot{\theta}_2-\dot{\theta}_1)^2, \tag{6}$$

which yields the generalized dissipative forces

$$-\frac{\partial\hat{\mathcal{R}}}{\partial\dot{\theta}_1}(\dot{q}) = -c(2\dot{\theta}_1-\dot{\theta}_2), \qquad -\frac{\partial\hat{\mathcal{R}}}{\partial\dot{\theta}_2}(\dot{q}) = -c(\dot{\theta}_2-\dot{\theta}_1), \qquad -\frac{\partial\hat{\mathcal{R}}}{\partial\dot{X}_\mathrm{c}}(\dot{q}) = 0. \tag{7}$$

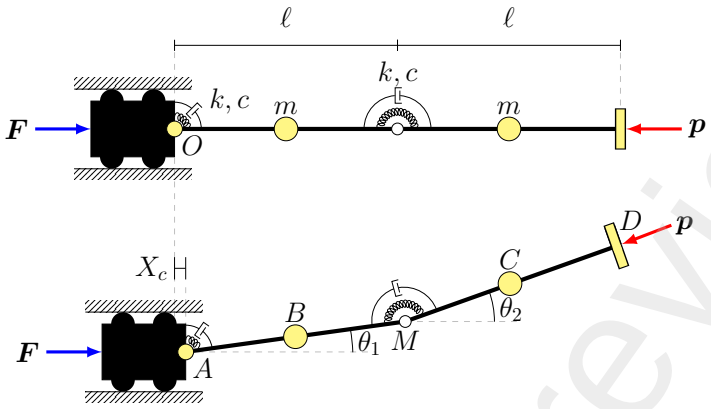

Figure 1: Sketch of the device introduced by Cazzolli et al. [3]. Upper part: the straight configuration ($\theta_1 = \theta_2 = 0$) with the cart located on the origin O, so that $X_c = 0$. Lower part: a deformed configuration ($\theta_1 \neq 0, \theta_2 \neq 0$), with the cart positioned at a point differing from the origin ($X_c \neq 0$). The hinges are characterized by an elastic stiffness $k > 0$ and a viscous damping coefficient $c > 0$. The reaction force $\boldsymbol{p}$ associated with the nonholonomic constraint (the 'wheel' or the 'skate') is directed along the axis of the bar $\mathscr{B}_2$.

The Lagrangian function $\mathcal{L}_o$ defined by Equation (5) describes, up to the dissipative terms, the 'original' device (whence the subscript 'o') as it was conceived by Cazzolli et al. [3]. Thus, it features the external potential FX_c. Moreover, it does not depend explicitly on time.

To determine the equations of motion for the considered system, we apply the *Extended Hamilton Method*, following Lanczos [21],

$$\delta \int_{t_{in}}^{t_{fin}} \hat{\mathcal{L}}_o(q,\dot{q})\,\mathrm{d}t = \int_{t_{in}}^{t_{fin}} \Big(\textstyle\sum_{\alpha=1}^{3} \dfrac{\partial \hat{\mathcal{R}}}{\partial \dot{q}_\alpha}(\dot{q}) \delta q_\alpha - \sum_{\alpha=1}^{3} \mu \dfrac{\partial \hat{\mathcal{C}}}{\partial \dot{q}_\alpha}(q,\dot{q})\,\delta q_\alpha \Big) \mathrm{d}t, \tag{8}$$

where the integral on the left-hand side is referred to as *action functional*, t_{in} and t_{fin} denote an initial and a final instant of time, and the function of time μ on the right-hand side is a Lagrange multiplier introduced to account for the nonholonomic constraint (4), see [21, 22, 23, 24] for details.

The variation of the action functional, performed as predicted by Hamilton's Principle, and under the hypothesis $\delta q_\alpha(t_{in}) = \delta q_\alpha(t_{fin}) = 0$ for $\alpha = 1, 2, 3$, leads to

$$\delta \int_{t_{in}}^{t_{fin}} \hat{\mathcal{L}}_o(q,\dot{q})\,\mathrm{d}t = \int_{t_{in}}^{t_{fin}} \textstyle\sum_{\alpha=1}^{3} (\mathscr{E}_\alpha \hat{\mathcal{L}}_o)\,\delta q_\alpha\,\mathrm{d}t, \tag{9}$$

with $\mathscr{E}_\alpha \hat{\mathcal{L}}_o$ being the Euler–Lagrange operator applied to $\hat{\mathcal{L}}_o$,

$$\mathscr{E}_\alpha \hat{\mathcal{L}}_o := \frac{\partial \hat{\mathcal{L}}_o}{\partial q_\alpha}(q,\dot{q}) - \frac{\mathrm{d}}{\mathrm{d}t}\Big(\frac{\partial \hat{\mathcal{L}}_o}{\partial \dot{q}_\alpha}(q,\dot{q})\Big), \qquad \alpha = 1,2,3. \tag{10}$$

Then, the local form of Equation (8) reads

$$\mathscr{E}_\alpha \hat{\mathcal{L}}_o - \frac{\partial \hat{\mathcal{R}}}{\partial \dot{q}_\alpha}(\dot{q}) + \mu \frac{\partial \hat{\mathcal{C}}}{\partial \dot{q}_\alpha}(q,\dot{q}) = 0, \qquad \alpha = 1,2,3. \tag{11}$$

The third term on the left-hand side of Equation (11) identifies, for $\alpha = 1, 2, 3$, the Lagrangian components of the reaction force due to the constraint, which are given by

$$\mu \frac{\partial \hat{C}}{\partial \dot{\theta}_1}(q, \dot{q}) = \mu \ell \sin(\theta_1 - \theta_2) \equiv \{\ell \hat{\boldsymbol{n}}_1(q) \times \hat{\boldsymbol{p}}(q)\} \cdot \boldsymbol{e}_3, \tag{12a}$$

$$\mu \frac{\partial \hat{C}}{\partial \dot{\theta}_2}(q, \dot{q}) \equiv \{\ell \hat{\boldsymbol{n}}_2(q) \times \hat{\boldsymbol{p}}(q)\} \cdot \boldsymbol{e}_3 = 0, \tag{12b}$$

$$\mu \frac{\partial \hat{C}}{\partial \dot{X}_\mathrm{c}}(q, \dot{q}) = -\mu \cos\theta_2 \equiv \hat{\boldsymbol{p}}(q) \cdot \boldsymbol{e}_1, \tag{12c}$$

where '$\times$' denotes the cross product and $\boldsymbol{p} = \hat{\boldsymbol{p}}(q) = -\mu \boldsymbol{n}_2$ is referred to as a *follower force* [3]. We notice that, in a generic configuration of the device, Equation (12a) is the (scalar) torque that the follower force exerts on $\mathscr{B}_1$ around the instantaneous position x_A of the point A. Similarly, Equation (12b) is the *null* (scalar) torque that $\boldsymbol{p}$ exerts on $\mathscr{B}_2$, since $\boldsymbol{p}$ is parallel to $\mathscr{B}_2$ by design. Moreover, Equation (12c) provides the $\boldsymbol{e}_1$-component of $\boldsymbol{p}$ acting on the cart.

3. Charged Ziegler's double-pendulum interacting with Lorentz force

With reference to the mechanical system described in the previous section and, in particular, to the Lagrangian function reported in Equation (5), we introduce here two *major modifications*:

(1) The massless wheel, concentrated at the point D (see Figure 1), carries *electric charge* $\mathfrak{e} \neq 0$ (it will be assumed $\mathfrak{e} > 0$ in the following);

(2) A solenoid $\mathscr{S}$ as described in detail in Section 3.1 is considered and two separate cases are analyzed: the device is placed in the interior of the solenoid (*Case I*); the device is placed in the exterior of the solenoid (*Case II*).

We refer the reader to Figure 2 for a graphical representation of the solenoid and of the device.

3.1. The paradigmatic solenoid problem and the Maxwell–Lodge effect

The solenoid $\mathscr{S}$ has virtually infinite height, axis parallel to $\boldsymbol{e}_3$, and circular cross section $\mathscr{C}$ of radius R_s much larger than 2ℓ. An electric current flowing in the wire constituting the solenoid generates a magnetic field $\boldsymbol{H}$, which, given the magnetic permeability of the vacuum μ_0, yields the magnetic induction field $\boldsymbol{B} = \mu_0 \boldsymbol{H}$.

Assuming appropriate regularity, the magnetic induction field $\boldsymbol{B}$ and the electric field $\boldsymbol{E}$ must fulfill the equations

$$\mathrm{div}\boldsymbol{B} = 0 \qquad \text{and} \qquad \mathrm{curl}\boldsymbol{E} = -\partial_t \boldsymbol{B}, \tag{13}$$

which constitute two of the four Maxwell equations written in local form. These conditions make it possible to express $\boldsymbol{B}$ and $\boldsymbol{E}$ in terms of a vector potential $\boldsymbol{A}$ and of a scalar potential Φ —both at least of class C^2— through the relations $\boldsymbol{B} = \mathrm{curl}\boldsymbol{A}$ and $\boldsymbol{E} = -\mathrm{grad}\,\Phi - \partial_t \boldsymbol{A}$ [25]. Because of the differential structure of these relations, the potentials $\boldsymbol{A}$ and Φ are not unique. Indeed, for any scalar field χ at least of class C^2, $\boldsymbol{B}$ and $\boldsymbol{E}$ remain invariant under transformations of the type

$$\boldsymbol{A} \mapsto \tilde{\boldsymbol{A}} = \boldsymbol{A} + \mathrm{grad}\,\chi, \qquad \Phi \mapsto \tilde{\Phi} = \Phi - \partial_t \chi, \tag{14}$$

known as *gauge transformations* [25]. The field χ is the *generator* of the gauge transformations and allows for obtaining new forms of the vector potential and of the scalar potential, therefore also referred to as *gauge potentials*.

Although the ideal solenoid considered in this section constitutes a paradigmatic and widely studied physical problem, we review it to contextualize it within the mechanical framework of the device presented in Section 2.

The solenoid problem is grounded on the fundamental hypothesis that the magnetic induction field $\boldsymbol{B}$ is non-null and homogeneous in the interior of $\mathscr{S}$ and identically null outside it, whence

$$\boldsymbol{B}(x,t) = B_{\mathrm{h}}(t)\,\boldsymbol{e}_3, \quad \text{for } x \in \mathrm{Int}(\mathscr{S}) \quad \text{and} \quad \boldsymbol{B}(x,t) = \boldsymbol{0}, \quad \text{for } x \in \mathbb{R}^3 \setminus \mathscr{S}, \tag{15}$$

where x is a spatial point of Cartesian coordinates (x_1, x_2, x_3), enumerated consistently with $\boldsymbol{e}_1$, $\boldsymbol{e}_2$, and $\boldsymbol{e}_3$, while $B_{\mathrm{h}}(t)$ is a prescribed function of time t [25].

We notice that the vanishing of $\boldsymbol{B}$ in the exterior of an ideal solenoid is exact *'in the stationary regime'* [17], although it can be maintained also under the hypothesis that the current flowing in the solenoid *'varies slowly in time'* [17]. The latter condition is fundamental in our setting and will be kept throughout the remainder of our work.

Within the so-called *temporal gauge* [26], which prescribes a vanishing scalar potential, the distribution of $\boldsymbol{B}$ given in Equation (15) and the relation $\boldsymbol{B} = \mathrm{curl}\boldsymbol{A}$ imply [25]

$$\boldsymbol{A}(x,t) = -\frac{1}{2}B_{\mathrm{h}}(t)x_2\,\boldsymbol{e}_1 + \frac{1}{2}B_{\mathrm{h}}(t)x_1\,\boldsymbol{e}_2, \qquad \Phi(x,t) = 0, \quad \text{in } \mathrm{Int}(\mathscr{S}), \tag{16a}$$

$$\boldsymbol{A}(x,t) = -\frac{1}{2}B_{\mathrm{h}}(t)R_{\mathrm{s}}^2\frac{x_2}{x_1^2+x_2^2}\,\boldsymbol{e}_1 + \frac{1}{2}B_{\mathrm{h}}(t)R_{\mathrm{s}}^2\frac{x_1}{x_1^2+x_2^2}\,\boldsymbol{e}_2, \qquad \Phi(x,t) = 0, \quad \text{in } \mathbb{R}^3 \setminus \mathscr{S}, \tag{16b}$$

with $\mathrm{Int}(\mathscr{S})$ being the set of internal points of $\mathscr{S}$. Therefore, $\boldsymbol{A}$ is continuous on $\partial\mathscr{S}$. Moreover, it is divergence free both in the interior and in the exterior of the solenoid, since the equality $\mathrm{div}\boldsymbol{A} = 0$ is identically satisfied both in $\mathrm{Int}(\mathscr{S})$ and in $\mathbb{R}^3 \setminus \mathscr{S}$, and it is irrotational outside the solenoid, since $\mathrm{curl}\boldsymbol{A} = \boldsymbol{0}$ in $\mathbb{R}^3 \setminus \mathscr{S}$.

It is worth recalling that the Euclidean norm of $\boldsymbol{A}(x,t)$ reads

$$\|\boldsymbol{A}(x,t)\| = \frac{1}{2}|B_{\mathrm{h}}(t)|\sqrt{x_1^2+x_2^2} = \frac{1}{2}|B_{\mathrm{h}}(t)|\,\|\boldsymbol{r}(x)\|, \qquad \text{in } \mathrm{Int}(\mathscr{S}), \tag{17a}$$

$$\|\boldsymbol{A}(x,t)\| = \frac{1}{2}|B_{\mathrm{h}}(t)|R_{\mathrm{s}}^2\frac{1}{\sqrt{x_1^2+x_2^2}} = \frac{1}{2}|B_{\mathrm{h}}(t)|\frac{R_{\mathrm{s}}^2}{\|\boldsymbol{r}(x)\|}, \qquad \text{in } \mathbb{R}^3 \setminus \mathscr{S}, \tag{17b}$$

with $\boldsymbol{r}(x) = x_1\boldsymbol{e}_1 + x_2\boldsymbol{e}_2$, thereby increasing linearly with $\varrho = \|\boldsymbol{r}(x)\|$ until $\varrho = R_{\mathrm{s}}$, and then decreasing asymptotically towards zero as ϱ^{-1} for $\varrho > R_{\mathrm{s}}$ [17, 25].

According to Equations (15), (16a), and (16b), for any open surface Σ with piecewise regular contour $\partial\Sigma$ lying on a plane that intersects transversely the solenoid, and either containing the cross section $\mathscr{C}$ of the solenoid or being equal to $\mathscr{C}$, the magnetic flux is

$$\Phi_{\mathrm{M}}(\Sigma;t) = \int_{\Sigma}\boldsymbol{B}(x,t)\cdot\boldsymbol{e}_3\,\mathrm{da}(x) = \int_{\partial\Sigma}\boldsymbol{A}(x,t)\cdot\boldsymbol{\tau}(x)\,\mathrm{d}s(x) = B_{\mathrm{h}}(t)\pi R_{\mathrm{s}}^2, \tag{18}$$

where $\boldsymbol{\tau}(x)$ is the unit vector tangent to $\partial\Sigma$ at x. When Σ contains $\mathscr{C}$, the magnetic induction field $\boldsymbol{B}$ is null in $\Sigma \setminus \mathscr{C}$ and the first integral in Equation (18) reduces to a surface integral over $\mathscr{C}$, whence $\Phi_{\mathrm{M}}(\Sigma;t) = B_{\mathrm{h}}(t)\pi R_{\mathrm{s}}^2$, with $\pi R_{\mathrm{s}}^2 = \mathrm{Area}(\mathscr{C})$. Since $\Phi_{\mathrm{M}}(\Sigma;t)$ must be independent of

$\Sigma \supseteq \mathscr{C}$, the magnetic flux can be obtained by directly computing the contour integral in Equation (18), with $\boldsymbol{A}$ given by Equation (16b) [25].

By employing Equations (16a) and (16b) for the calculation of the electric field within the *temporal gauge* ($\Phi = 0$), which implies $\boldsymbol{E} = -\mathrm{grad}\Phi - \partial_t \boldsymbol{A} = -\partial_t \boldsymbol{A}$, we obtain

$$\boldsymbol{E}(x,t) = \frac{1}{2}\dot{B}_{\mathrm{h}}(t) x_2\, \boldsymbol{e}_1 - \frac{1}{2}\dot{B}_{\mathrm{h}}(t) x_1\, \boldsymbol{e}_2, \qquad \text{in } \mathrm{Int}(\mathscr{S}), \tag{19a}$$

$$\boldsymbol{E}(x,t) = \frac{1}{2}\dot{B}_{\mathrm{h}}(t) R_{\mathrm{s}}^2 \frac{x_2}{x_1^2 + x_2^2}\, \boldsymbol{e}_1 - \frac{1}{2}\dot{B}_{\mathrm{h}}(t) R_{\mathrm{s}}^2 \frac{x_1}{x_1^2 + x_2^2}\, \boldsymbol{e}_2, \qquad \text{in } \mathbb{R}^3 \setminus \mathscr{S}. \tag{19b}$$

A consequence of Equations (19a) and (19b) is the Lorentz force exerted on the charged skate placed at the end-point D of the bar $\mathscr{B}_2$ of the device under study. In this respect, as mentioned at the beginning of this section, we consider the following two difference cases (Figure 2):

Case I: Device inside the solenoid. If the cross section of the solenoid is big enough to host the device, and if we assume that the motion of the device remains confined to this cross section, so that the skate does not transit through the lateral boundary of the solenoid, then the Lorentz force acting on the skate in $\mathrm{Int}(\mathscr{S})$ reads

$$\begin{aligned}\boldsymbol{F}_{\mathrm{L}}(x_D(t),t) =& \mathfrak{e}\,[\boldsymbol{E}(x_D(t),t) + \boldsymbol{v}_D(t) \times \boldsymbol{B}(x_D(t),t)] \\ =& \left(\frac{\mathfrak{e}\dot{B}_{\mathrm{h}}(t)}{2}\, x_{D2}(t) + \mathfrak{e} B_{\mathrm{h}}(t)\dot{x}_{D2}(t)\right)\boldsymbol{e}_1 - \left(\frac{\mathfrak{e}\dot{B}_{\mathrm{h}}(t)}{2}\, x_{D1}(t) + \mathfrak{e} B_{\mathrm{h}}(t)\dot{x}_{D1}(t)\right)\boldsymbol{e}_2,\end{aligned} \tag{20}$$

meaning that it consists both of an electric and of a magnetic contribution. Note that the fields $\boldsymbol{E}$ and $\boldsymbol{B}$ are defined at all spatial points, and, consequently, they couple dynamically with the system through their evaluation at time t and at the spatial point $x = x_D(t)$ occupied by the material point D at the same time.

For this reason, the Lorentz force is evaluated at $x = x_D(t)$, with velocity $\boldsymbol{v}_D(t)$ at time t. The same considerations apply to the vector potential $\boldsymbol{A}$.

Case II: Device outside the solenoid. The nontrivial electric field present also in the exterior of the solenoid, as given by Equation (19b), generates a Lorentz force acting on the charged skate, even in the case in which the skate is located outside the solenoid. In this setting, the Lorentz force in $\mathbb{R}^3 \setminus \mathscr{S}$ reads

$$\begin{aligned}\boldsymbol{F}_{\mathrm{L}}(x_D(t),t) &= \mathfrak{e}\,\boldsymbol{E}(x_D(t),t) \\ &= \frac{\mathfrak{e}\dot{B}_{\mathrm{h}}(t)R_{\mathrm{s}}^2}{2}\frac{x_{D2}(t)}{[x_{D1}(t)]^2 + [x_{D2}(t)]^2}\,\boldsymbol{e}_1 - \frac{\mathfrak{e}\dot{B}_{\mathrm{h}}(t)R_{\mathrm{s}}^2}{2}\frac{x_{D1}(t)}{[x_{D1}(t)]^2 + [x_{D2}(t)]^2}\,\boldsymbol{e}_2.\end{aligned} \tag{21}$$

Remark 1 (The Maxwell–Lodge effect revisited)**.**
Equations (16b) *and* (19b) *evidence that the vector potential* $\boldsymbol{A}$ *and the electric field* $\boldsymbol{E} = -\partial_t \boldsymbol{A}$ *are non-null also outside the solenoid, where the magnetic induction field* $\boldsymbol{B}$ *is null. This result has many important physical consequences, one of which is known as* Maxwell–Lodge effect *[18]: by positioning a coil of given electric conductivity around the solenoid, but not in contact with it, an electric current flowing in this coil is observed in response to the electromotive force generated by the negative of the time derivative of the magnetic flux* $B_{\mathrm{h}}(t)\pi R_{\mathrm{s}}^2$*, due to* $\boldsymbol{B}$ *inside the solenoid [17]. While this result is exactly the Faraday–Neumann–Lenz law, with the electromotive force being* $\mathscr{E}(t) := \int_{\partial\Sigma} \boldsymbol{E}(x,t)\cdot\boldsymbol{\tau}(x)\,\mathrm{d}s(x) = -\dot{B}_{\mathrm{h}}(t)\pi R_{\mathrm{s}}^2$*, and* $\partial\Sigma$ *representing the coil*

—assumed filiform—, the fact that the current in the coil occurs in the region of space in which the magnetic flux is null (but $\boldsymbol{E} = -\partial_t \boldsymbol{A}$ is non-null) constitutes the essence of the Maxwell–Lodge effect. This has generated considerable debate aiming at clarifying the role and intrinsic meaning of the vector potential $\boldsymbol{A}$ in classical physics. Although reviewing the 'paradoxes and controversies around the Maxwell–Lodge effect' *[17] is out of the scopes of our work (the interested reader is referred to [17]), we argue here that the Maxwell–Lodge effect manifests itself also in the dynamics of the charged Ziegler double pendulum in Case II, when the pendulum is placed outside the solenoid. Indeed, because of the electric charge* $\mathfrak{e}$ *concentrated at the point D of the device, this point is subject to the Lorentz force* $\boldsymbol{F}_{\mathrm{L}}(x_D(t), t)$ *as prescribed by Equation* (21) *when the device is in* $\mathbb{R}^3 \setminus \mathscr{S}$*. In turn,* $\boldsymbol{F}_{\mathrm{L}}(x_D(t), t)$ *influences the dynamics of the device and interacts with the dead load F applied to the cart, at least until the device exceeds a certain distance from the solenoid's boundary, beyond which the amplitude of* $\boldsymbol{F}_{\mathrm{L}}(x_D(t), t)$*, decreasing radially as* $\{[x_{D1}(t)]^2 + [x_{D2}(t)]^2\}^{-1/2}$*, becomes negligible compared to F.*

On the basis of well documented results on the gauge transformations presented in Equation (14) [25], one can choose the generators

$$\chi(x,t) = \tfrac{1}{2} B_{\mathrm{h}}(t) x_1 x_2, \qquad \text{in } \mathrm{Int}(\mathscr{S}), \tag{22a}$$

$$\chi(x,t) = \tfrac{1}{2} B_{\mathrm{h}}(t) R_{\mathrm{s}}^2 \arctan(x_1/x_2), \qquad \text{in } \mathbb{R}^3 \setminus \mathscr{S} \text{ and for } x_2 \neq 0, \tag{22b}$$

thereby moving out from the temporal gauge and switching to the transformed gauge potentials

$$\tilde{\boldsymbol{A}}(x,t) = B_{\mathrm{h}}(t) x_1 \, \boldsymbol{e}_2, \quad \tilde{\Phi}(x,t) = -\tfrac{1}{2} \dot{B}_{\mathrm{h}}(t) x_1 x_2, \qquad \text{in } \mathrm{Int}(\mathscr{S}), \tag{23a}$$

$$\tilde{\boldsymbol{A}}(x,t) = \boldsymbol{0}, \qquad \tilde{\Phi}(x,t) = -\tfrac{1}{2} \dot{B}_{\mathrm{h}}(t) R_{\mathrm{s}}^2 \arctan(x_1/x_2), \quad \text{in } \mathbb{R}^3 \setminus \mathscr{S} \text{ and for } x_2 \neq 0 \tag{23b}$$

(note that χ has null Laplacian in the region in which it is defined). The new gauge potentials, however, yield exactly the same Lorentz forces as those reported in Equations (20) and (21), with the only (irrelevant) technical difference being that $\boldsymbol{B}$ and $\boldsymbol{E}$ are now to be computed as $\boldsymbol{B} = \mathrm{curl}\tilde{\boldsymbol{A}}$ and $\boldsymbol{E} = -\mathrm{grad}\,\tilde{\Phi} - \partial_t \tilde{\boldsymbol{A}}$. In particular, outside the solenoid, $\boldsymbol{E} = -\mathrm{grad}\,\tilde{\Phi}$ holds at all points $x \in \mathbb{R}^3 \setminus \mathscr{S}$ such that $x_2 \neq 0$. Therefore, for any open surface $\Sigma \supset \mathscr{C}$ having piecewise regular contour $\partial\Sigma$, $\boldsymbol{E}$ is undefined at both points in which $\partial\Sigma$ intersects the x_1-axis. However, since these two points constitute a set of null measure, the electromotive force $\mathscr{E}(t) = -\int_{\partial\Sigma} \mathrm{grad}\,\tilde{\Phi}(x,t) \cdot \boldsymbol{\tau}(x)\, \mathrm{d}s(x)$ remains unchanged and delivers $-\dot{B}_{\mathrm{h}}(t)\pi R_{\mathrm{s}}^2$, as is the case of the temporal gauge.

3.2. The Lagrangian function of the charged Ziegler double pendulum

The Lagrangian function of the device subjected to the additional magnetic interaction is obtained from the Lagrangian function $\mathcal{L}_{\mathrm{o}}$ in Equation (5) by adding the generalized, velocity-dependent potential $\mathfrak{e}\boldsymbol{A}(x_D(t), t) \cdot \boldsymbol{v}_D(t)$, in which $\boldsymbol{A}$ is evaluated at time t and at the spatial point $x_D(t)$ that is instantaneously occupied by the moving charge at time t [20, 25]. In terms of the system's Lagrangian parameters and generalized velocities, this yields (see also [19] for the case of the *'knife edge with a dipole moment in a magnetic field'*)

$$\mathcal{L} \equiv \hat{\mathcal{L}}(q, \dot{q}, t) = \hat{\mathcal{L}}_{\mathrm{o}}(q, \dot{q}) + \mathfrak{e}[\mathcal{A}_1(q,t)\dot{\theta}_1 + \mathcal{A}_2(q,t)\dot{\theta}_2 + \mathcal{A}_3(q,t)\dot{X}_{\mathrm{c}}], \tag{24}$$

where, for $\beta = 1, 2, 3$, the functions $\mathcal{A}_\beta(q,t) = \frac{1}{2} B_\mathrm{h}(t) \mathcal{U}_\beta(q) \ell^2$ express explicitly how the device interacts with the vector potential and are defined by the auxiliary quantities

$$\mathcal{U}_1(q) \coloneqq \begin{cases} 1 + \cos(\theta_2 - \theta_1) + (X_\mathrm{c}/\ell)\cos\theta_1 & \text{Case I} \\ \dfrac{R_\mathrm{s}^2}{\ell^2} \dfrac{1 + \cos(\theta_2 - \theta_1) + (X_\mathrm{c}/\ell)\cos\theta_1}{[\cos\theta_1 + \cos\theta_2 + (X_\mathrm{c}/\ell)]^2 + [\sin\theta_1 + \sin\theta_2]^2} & \text{Case II} \end{cases} \tag{25a}$$

$$\mathcal{U}_2(q) \coloneqq \begin{cases} 1 + \cos(\theta_2 - \theta_1) + (X_\mathrm{c}/\ell)\cos\theta_2 & \text{Case I} \\ \dfrac{R_\mathrm{s}^2}{\ell^2} \dfrac{1 + \cos(\theta_2 - \theta_1) + (X_\mathrm{c}/\ell)\cos\theta_2}{[\cos\theta_1 + \cos\theta_2 + (X_\mathrm{c}/\ell)]^2 + [\sin\theta_1 + \sin\theta_2]^2} & \text{Case II} \end{cases} \tag{25b}$$

$$\mathcal{U}_3(q) \coloneqq \begin{cases} -\dfrac{\sin\theta_1 + \sin\theta_2}{\ell} & \text{Case I} \\ -\dfrac{R_\mathrm{s}^2}{\ell^3} \dfrac{\sin\theta_1 + \sin\theta_2}{[\cos\theta_1 + \cos\theta_2 + (X_\mathrm{c}/\ell)]^2 + [\sin\theta_1 + \sin\theta_2]^2} & \text{Case II.} \end{cases} \tag{25c}$$

More in detail, it can be shown that, both in Case I and in Case II, the following identifications apply:

$$\mathcal{A}_1(q(t),t) = [\ell \boldsymbol{n}_1(t) \times \boldsymbol{A}(x_D(t),t)] \cdot \boldsymbol{e}_3, \tag{26a}$$

$$\mathcal{A}_2(q(t),t) = [\ell \boldsymbol{n}_2(t) \times \boldsymbol{A}(x_D(t),t)] \cdot \boldsymbol{e}_3, \tag{26b}$$

$$\mathcal{A}_3(q(t),t) = \boldsymbol{A}(x_D(t),t) \cdot \boldsymbol{e}_1. \tag{26c}$$

We remark that the vector potential $\boldsymbol{A}$, although having only two nonzero components, generates the three nonzero components $\mathcal{A}_1$, $\mathcal{A}_2$, and $\mathcal{A}_3$, with the first two being conjugate to the angular velocities of the bars $\dot\theta_1$ of $\dot\theta_2$, and the last one being conjugate to the linear velocity $\dot X_\mathrm{c}$ of the cart along the $\boldsymbol{e}_1$-axis. In addition, functions $\mathcal{A}_1$, $\mathcal{A}_2$, and $\mathcal{A}_3$, explained in Equations (26a)–(26c), describe how the vector potential couples at each instant of time t with the configuration $q(t)$ assumed by the system as a whole at time t.

We emphasize that the charge of the skate is assumed to be sufficiently weak so that the magnetic and the electric fields that it generates can be neglected.

A major difference with respect to the work by Cazzolli et al. [3] is that, in addition to the dead load applied to the cart, the system is also subjected to the *Lorentz force* $\boldsymbol{F}_\mathrm{L}(x_D(t),t)$, which assumes the expression given in Equation (20) or in Equation (21), depending on whether the device is inside or outside the solenoid, respectively.

In Case I, and when $\boldsymbol{A}$ does not depend explicitly on time, the Lorentz force reduces to $\boldsymbol{F}_\mathrm{L}(x_D(t),t) = \mathfrak{e}\, \boldsymbol{v}_D(t) \times \boldsymbol{B}(x_D(t))$ and, because of the constraint (4), it remains parallel to the bar $\mathscr{B}_2$, and thus with the follower force $\boldsymbol{p} = -\mu \boldsymbol{n}_2$, at all times. In addition, the Lorentz force vanishes whenever $\boldsymbol{v}_D(t)$ is null.

In Case II, the Lorentz force features solely the purely electric contribution, which is due to the explicit time dependence of $\boldsymbol{A}$, that is, $\boldsymbol{F}_\mathrm{L}(x_D(t),t) = \mathfrak{e}\boldsymbol{E}(x_D(t),t) = -\mathfrak{e}\, \partial_t \boldsymbol{A}(x_D(t),t)$. Therefore, if $\boldsymbol{A}$ is assumed to not be explicitly dependent on time, then the Lorentz force vanishes identically.

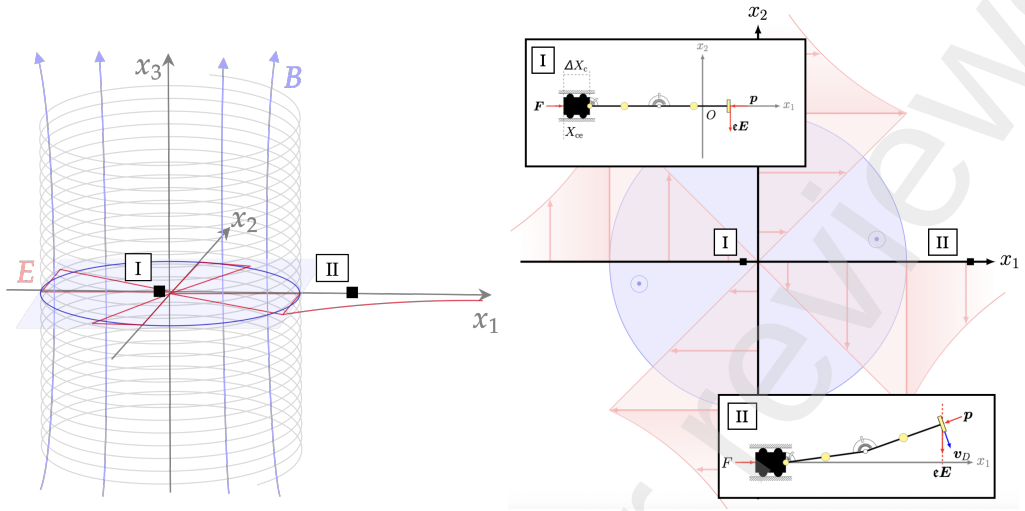

Figure 2: Sketch of the solenoid, illustrating the electric field $\boldsymbol{E}$ (red) and the magnetic induction field $\boldsymbol{B}$ (blue). The system is shown both in a three-dimensional perspective and in a vertical cross-section, with the device positions for Case I and Case II indicated in both views. In the position referring to Case I, $\Delta X_c := X_{c0} - X_{ce}$, with X_{c0} being the initial position of the cart. The images correspond to assuming $B_h(t) > 0$ and $\dot{B}_h(t) > 0$. In the zoomed-in image referring to Case II, $\mathfrak{e}\boldsymbol{E}$ is directed tangentially to the circumference centered in O and passing through D, but it can be regarded as approximately parallel to the x_2-axis because the device is placed at a relatively long distance from O.

3.3. Dynamic equations

If the dynamic equations (11), featuring the Lagrangian function $\hat{\mathcal{L}}_o$, are written explicitly, they lead to the set of equations presented by Cazzolli et al. [3]. In our framework, however, since electromagnetic interactions are considered, the dynamic equations follow from the Lagrangian function $\hat{\mathcal{L}}$ expressed in Equation (24). They read

$$\mathscr{E}_\alpha \hat{\mathcal{L}} - \frac{\partial \hat{\mathcal{R}}}{\partial \dot{q}_\alpha}(\dot{q}) + \mu \frac{\partial \hat{C}}{\partial \dot{q}_\alpha}(q, \dot{q}) = 0, \qquad \alpha = 1, 2, 3, \tag{27}$$

where, as in Equation (11), the contributions $-\partial_{\dot{q}_\alpha}\hat{\mathcal{R}}(\dot{q})$ and $\mu\, \partial_{\dot{q}_\alpha}\hat{C}(q, \dot{q})$ identify the dissipative generalized forces associated with damping and the reaction forces due to the nonholonomic *"skate' constraint'* [3], respectively.

Before deriving the new Euler–Lagrange equations, we notice that the Euler–Lagrange operator applied to $\hat{\mathcal{L}}$ produces

$$\mathscr{E}_\alpha \hat{\mathcal{L}} = \mathscr{E}_\alpha \hat{\mathcal{L}}_o + \mathfrak{e} \sum_{\beta=1}^{3} \mathcal{F}_{\alpha\beta}\, \dot{q}_\beta + \mathfrak{e}\, \mathcal{E}_\alpha, \qquad \alpha = 1, 2, 3, \tag{28}$$

where the quantities $\mathcal{F}_{\alpha\beta}$ and $\mathcal{E}_\alpha$ are defined as

$$\mathcal{F}_{\alpha\beta} := \frac{\partial \mathcal{A}_\beta}{\partial q_\alpha} - \frac{\partial \mathcal{A}_\alpha}{\partial q_\beta}, \qquad \mathcal{E}_\alpha := -\frac{\partial \mathcal{A}_\alpha}{\partial t} \qquad \alpha, \beta = 1, 2, 3, \tag{29}$$

and represent, in terms of the Lagrangian parameters selected, the components of the *generalized Faraday tensor* and of the *generalized electric field*, respectively. From the discussion in Section 3.1, in which the electric and the magnetic contributions of the Lorentz force have been analyzed

in Cartesian coordinates, it follows that the magnetic contribution is active only in the interior of the solenoid. Accordingly, the equations of motion either include or exclude the magnetic contribution of the Lorentz force, depending on whether the device is located inside or outside the solenoid (Case I and Case II, respectively). Since this result must be consistently described when the device is analyzed in terms of the components of the generalized Faraday tensor and of the generalized electric field, defined by Equation (29), the quantities $\mathcal{F}_{\alpha\beta}$ must vanish identically in Case II, when the device moves outside the solenoid.

Specifically, the generalized Faraday tensor has components

$$\mathcal{F}_{12} = -\ell^2 B_{\rm h}(t)\sin(\theta_1-\theta_2), \quad \mathcal{F}_{13} = -\ell B_{\rm h}(t)\cos\theta_1, \quad \mathcal{F}_{23} = -\ell B_{\rm h}(t)\cos\theta_2, \quad \text{Case I} \tag{30a}$$

$$\mathcal{F}_{12} = 0, \quad \mathcal{F}_{13} = 0, \quad \mathcal{F}_{23} = 0, \quad \text{Case II} \tag{30b}$$

with $\mathcal{F}_{\alpha\beta} = -\mathcal{F}_{\beta\alpha}$ for $\alpha,\beta = 1,2,3$, while the generalized electric field has components

$$\mathcal{E}_\alpha \equiv -\partial_t \mathcal{A}_\alpha = -\tfrac{1}{2}\dot{B}_{\rm h}(t)\mathcal{U}_\alpha(q)\ell^2, \quad \alpha = 1,2,3, \tag{31}$$

where functions $\mathcal{U}_\alpha(q)$ are given in Equations (25a)–(25c), depending on whether Case I or Case II is considered.

Finally, upon introducing the components of the generalized Lorentz force

$$\mathfrak{F}_{{\rm L}\alpha} \coloneqq \mathfrak{e}\sum_{\beta=1}^{3}\mathcal{F}_{\alpha\beta}\,\dot{q}_\beta + \mathfrak{e}\,\mathcal{E}_\alpha, \quad \alpha = 1,2,3, \tag{32}$$

the dynamic equations (27) read

$$\mathscr{E}_\alpha\hat{\mathcal{L}}_{\rm o} - \frac{\partial\hat{\mathcal{R}}}{\partial\dot{q}_\alpha}(\dot{q}) + \mu\frac{\partial\hat{\mathcal{C}}}{\partial\dot{q}_\alpha}(q,\dot{q}) + \mathfrak{F}_{{\rm L}\alpha} = 0, \qquad \alpha = 1,2,3, \tag{33}$$

and, in explicit form, they become

$$\begin{aligned}&\tfrac{5}{4}m\ell^2\,\ddot{\theta}_1 + \tfrac{1}{2}m\ell^2\cos(\theta_1-\theta_2)\ddot{\theta}_2 - \tfrac{3}{2}m\ell(\sin\theta_1)\ddot{X}_{\rm c} + \tfrac{1}{2}m\ell^2\sin(\theta_1-\theta_2)\dot{\theta}_2^2\\ &= -k(2\theta_1-\theta_2) - c(2\dot{\theta}_1-\dot{\theta}_2) + \mu\ell\sin(\theta_1-\theta_2) + \mathfrak{F}_{\rm L1},\end{aligned} \tag{34a}$$

$$\begin{aligned}&\tfrac{1}{2}m\ell^2\cos(\theta_1-\theta_2)\ddot{\theta}_1 + \tfrac{1}{4}m\ell^2\ddot{\theta}_2 - \tfrac{1}{2}m\ell(\sin\theta_2)\ddot{X}_{\rm c} - \tfrac{1}{2}m\ell^2\sin(\theta_1-\theta_2)\dot{\theta}_1^2\\ &= -k(\theta_2-\theta_1) - c(\dot{\theta}_2-\dot{\theta}_1) + \mathfrak{F}_{\rm L2},\end{aligned} \tag{34b}$$

$$\begin{aligned}&-\tfrac{3}{2}m\ell(\sin\theta_1)\ddot{\theta}_1 - \tfrac{1}{2}m\ell(\sin\theta_2)\ddot{\theta}_2 + M\ddot{X}_{\rm c} - \tfrac{3}{2}m\ell(\cos\theta_1)\dot{\theta}_1^2 - \tfrac{1}{2}m\ell(\cos\theta_2)\dot{\theta}_2^2\\ &= -\mu\cos\theta_2 + F + \mathfrak{F}_{\rm L3}.\end{aligned} \tag{34c}$$

where, together with the total mass $M \coloneqq 2m + m_{\rm c}$, the explicit expressions for the generalized components of the Lorentz force are introduced:

$$\mathfrak{F}_{\rm L1} = \begin{cases} -\tfrac{1}{2}\mathfrak{e}\dot{B}_{\rm h}(t)\mathcal{U}_1(q)\ell^2 - \mathfrak{e}B_{\rm h}(t)[\sin(\theta_1-\theta_2)\dot{\theta}_2 + (\cos\theta_1)(\dot{X}_{\rm c}/\ell)]\ell^2 & \text{Case I}\\ -\tfrac{1}{2}\mathfrak{e}\dot{B}_{\rm h}(t)\mathcal{U}_1(q)\ell^2 & \text{Case II,}\end{cases} \tag{35a}$$

$$\mathfrak{F}_{\rm L2} = \begin{cases} -\tfrac{1}{2}\mathfrak{e}\dot{B}_{\rm h}(t)\mathcal{U}_2(q)\ell^2 + \mathfrak{e}B_{\rm h}(t)[\sin(\theta_1-\theta_2)\dot{\theta}_1 - (\cos\theta_2)(\dot{X}_{\rm c}/\ell)]\ell^2 & \text{Case I}\\ -\tfrac{1}{2}\mathfrak{e}\dot{B}_{\rm h}(t)\mathcal{U}_2(q)\ell^2 & \text{Case II,}\end{cases} \tag{35b}$$

$$\mathfrak{F}_{\rm L3} = \begin{cases} -\tfrac{1}{2}\mathfrak{e}\dot{B}_{\rm h}(t)\mathcal{U}_3(q)\ell^2 + \mathfrak{e}B_{\rm h}(t)[(\cos\theta_1)\dot{\theta}_1 + (\cos\theta_2)\dot{\theta}_2]\ell & \text{Case I}\\ -\tfrac{1}{2}\mathfrak{e}\dot{B}_{\rm h}(t)\mathcal{U}_3(q)\ell^2 & \text{Case II.}\end{cases} \tag{35c}$$

We emphasize that the magnetic part of the generalized force component in Equation (35b) is zero also in Case I since the terms in square brackets return the constraint (4). This is because the magnetic part of the Lorentz force $\mathfrak{e}\boldsymbol{v}_D \times \boldsymbol{B}$ is parallel to the bar of unit vector $\boldsymbol{n}_2$ and also with the follower force, as explained at the end of Section 2.

Equations (34a)–(34c) are to be solved together with the constraint (4), which we differentiate with respect to time and turn into the second-order differential equation

$$-\ell \sin(\theta_1 - \theta_2)\ddot{\theta}_1 + (\cos\theta_2)\ddot{X}_\mathrm{c} = \dot{\theta}_2\dot{X}_\mathrm{c}\sin\theta_2 + \ell\dot{\theta}_1\cos(\theta_1 - \theta_2)(\dot{\theta}_1 - \dot{\theta}_2). \tag{36}$$

Equation (36), obtained by changing sign to the time derivative of Equation (4), is necessary to apply Schur's complement technique to the system (34a)–(34c) and (36) (see [20, 27] for details; the sign change is motivated by convenience in the construction of the Schur matrix).

Alongside the elastic and viscous forces featuring in the right-hand sides of Equations (34a)–(34c), the additional generalized Lorentz forces $\mathfrak{F}_{\mathrm{L}1}$, $\mathfrak{F}_{\mathrm{L}2}$ and $\mathfrak{F}_{\mathrm{L}3}$ are present, and, coherently with Equations (12a)–(12c), the following identifications apply

$$\mathfrak{F}_{\mathrm{L}1} = [\ell\boldsymbol{n}_1(t) \times \boldsymbol{F}_\mathrm{L}(x_D(t), t)] \cdot \boldsymbol{e}_3, \tag{37a}$$

$$\mathfrak{F}_{\mathrm{L}2} = [\ell\boldsymbol{n}_2(t) \times \boldsymbol{F}_\mathrm{L}(x_D(t), t)] \cdot \boldsymbol{e}_3, \tag{37b}$$

$$\mathfrak{F}_{\mathrm{L}3} = \boldsymbol{F}_\mathrm{L}(x_D(q), t) \cdot \boldsymbol{e}_1. \tag{37c}$$

Equations (37a) and (37b) are the torques generated by the Lorentz force acting on the bars $\mathscr{B}_1$ and $\mathscr{B}_2$, respectively, while Equation (37c) is the component of the Lorentz force acting on the cart.

3.4. Determination of static equilibrium

To study the static equilibrium of the system, we consider an initial instant of time t_0 at which the system occupies the configuration $q(t_0) = q_0$, with null velocity $\dot{q}(t_0)$, and, for $t > t_0$, we look for solutions to Equations (34a)–(34c) of the type $q(t) = q_\mathrm{e} := (\theta_{1\mathrm{e}}, \theta_{2\mathrm{e}}, X_{\mathrm{ce}}) \equiv q_0$, satisfying $\dot{q}(t) = (0, 0, 0)$ and

$$-\mu_\mathrm{e}\ell\sin(\theta_{1\mathrm{e}} - \theta_{2\mathrm{e}}) = -\tfrac{1}{2}\mathfrak{e}\dot{B}_\mathrm{h}(t)\mathcal{U}_1(q_\mathrm{e})\ell^2 - k(2\theta_{1\mathrm{e}} - \theta_{2\mathrm{e}}), \tag{38a}$$

$$0 = -\tfrac{1}{2}\mathfrak{e}\dot{B}_\mathrm{h}(t)\mathcal{U}_2(q_\mathrm{e})\ell^2 - k(\theta_{2\mathrm{e}} - \theta_{1\mathrm{e}}), \tag{38b}$$

$$\mu_\mathrm{e}\cos\theta_{2\mathrm{e}} = -\tfrac{1}{2}\mathfrak{e}\dot{B}_\mathrm{h}(t)\mathcal{U}_3(q_\mathrm{e})\ell^2 + F, \tag{38c}$$

where μ_e is the (for the moment unknown) Lagrange multiplier at equilibrium [24, p. 25].

Note that the nonholonomic constraint (4) is trivially satisfied when the generalized velocities are all set equal to zero. For this reason, the number of equations characterizing equilibrium reduces to the three force balances (38a)–(38c), which, however, still feature the four unknowns $\theta_{1\mathrm{e}}$, $\theta_{2\mathrm{e}}$, X_{ce}, and μ_e. We also notice that the torques due to the magnetic part of the Lorentz force are not present in Equations (38a)–(38c) because the velocities are set equal to zero.

Assuming $\theta_{1\mathrm{e}} = \theta_{1\mathrm{e}} = \theta_\mathrm{e}$, Equations (38a)–(38c) become

$$0 = -\tfrac{1}{2}\mathfrak{e}\dot{B}_\mathrm{h}(t)\mathcal{U}_1(q_\mathrm{e})\ell^2 - k\theta_\mathrm{e}, \tag{39a}$$

$$0 = -\tfrac{1}{2}\mathfrak{e}\dot{B}_\mathrm{h}(t)\mathcal{U}_2(q_\mathrm{e})\ell^2, \tag{39b}$$

$$\mu_{\mathrm{e}} \cos\theta_{\mathrm{e}} = -\tfrac{1}{2}\mathfrak{e}\dot{B}_{\mathrm{h}}(t)\mathcal{U}_3(q_{\mathrm{e}})\ell^2 + F, \tag{39c}$$

with $\mathcal{U}_1(q_{\mathrm{e}}) = \mathcal{U}_2(q_{\mathrm{e}})$. Thus, equilibrium in the general case in which $\dot{B}_{\mathrm{h}}(t)$ is different from zero requires from Equation (39b) $\mathcal{U}_2(q_{\mathrm{e}}) = 0$, which may hold true only in Case I. Hence, we find

$$\mathcal{U}_2(q_{\mathrm{e}}) = 0 \qquad \Rightarrow \qquad 2 + \frac{X_{\mathrm{ce}}}{\ell}\cos\theta_{\mathrm{e}} = 0 \qquad \Rightarrow \qquad X_{\mathrm{ce}} = -\frac{2\ell}{\cos\theta_{\mathrm{e}}}. \tag{40}$$

Moreover, since $\mathcal{U}_1(q_{\mathrm{e}})$ vanishes too, Equation (39a) yields the more stringent condition

$$\theta_{\mathrm{e}} = 0. \tag{41}$$

This implies that $\mathcal{U}_3(q_{\mathrm{e}})$ also vanishes identically, thereby yielding the force balance

$$\mu_{\mathrm{e}} = F. \tag{42}$$

By gathering the results (40)–(42), we find

$$q_{\mathrm{e}} = (\theta_{1\mathrm{e}}, \theta_{2\mathrm{e}}, X_{\mathrm{ce}}) = (0, 0, -2\ell), \qquad \mu_{\mathrm{e}} = F. \tag{43}$$

The condition $\mathcal{U}_1(q_{\mathrm{e}}) = \mathcal{U}_2(q_{\mathrm{e}}) = 0$ for nonzero $\dot{B}_{\mathrm{h}}(t)$ amounts to placing the device in a configuration in which the electric part $\mathfrak{e}\boldsymbol{E}$ of the Lorentz force acting on the massless wheel is null (see Figure 3a). Indeed, given the expression $\mathfrak{e}\boldsymbol{E}(\hat{x}_D(q_{\mathrm{e}}), t) = -\frac{1}{2}\mathfrak{e}\dot{B}_{\mathrm{h}}(t)(X_{\mathrm{ce}} + 2\ell)\boldsymbol{e}_2$, the requirement of the vanishing of this force means that the skate has to occupy the origin of the considered reference frame, where $\hat{x}_D(q_{\mathrm{e}}) = 0$ and, thus, $X_{\mathrm{ce}} = -2\ell$.

We note that no equilibrium configuration exists in Case II, since, when the device is outside the solenoid, Equation (39b) cannot be satisfied unless the trivial condition of time independent B_{h} is considered. On the other hand, if $\dot{B}_{\mathrm{h}}(t) = 0$ for all $t \geq t_0$, every triple $(\theta_1(t), \theta_2(t), X_{\mathrm{c}}(t)) = (0, 0, X_{\mathrm{ce}})$, with arbitrary $X_{\mathrm{ce}} > R_{\mathrm{s}}$, satisfies the equilibrium conditions.

See Figure 3 for a graphical depiction of the device in the four configurations of interest inside the solenoid (Case I).

Remark 2 (One static equilibrium configuration extracted from the manifold in [3])**.**
The configuration q_{e} determined in Equation (43) *is* one *particular configuration of the manifold* $\{(0, 0, X_{\mathrm{ce}}) : \ X_{\mathrm{ce}} \in \mathbb{R}\}$ *of equilibrium configurations obtained in [3] in the absence of magnetic interactions. This constitutes an important difference from the work by Cazzolli et al. [3]. In our setting, indeed, X_{c} cannot be arbitrary, since the equilibrium configuration is obtained by imposing the additional condition of null electric part of the Lorentz force acting on the skate. However, we retrieve the same equilibrium manifold as Cazzolli et al. [3] if we assume that B_{h} is independent of time, which implies $\dot{B}_{\mathrm{h}}(t) = 0$ at all times. Indeed, under the hypothesis of time-independent B_{h}, Equation* (39a) *returns $\theta_{\mathrm{e}} = 0$, Equation* (39b) *is trivially satisfied (thus, there is no counterpart of Equation* (40) *to determine X_{ce}, which remains unprescribed), and Equation* (39c) *reduces to $\mu_{\mathrm{e}} = F$.*

4. Stability analysis: flutter instability and bifurcations in Case I

In this section, we carry out a stability analysis of the system described by Equations (34a)–(34c) and (36). To this end, since we need to perturb the system from a static equilibrium configuration, we restrict our study to Case I only. For the methodologies used hereafter, we refer to [3, 6, 23, 28].

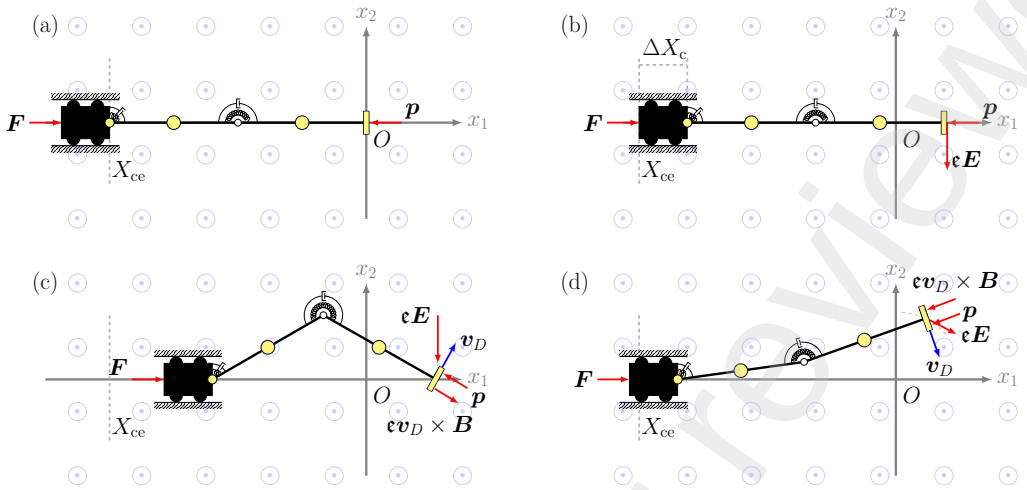

Figure 3: Body diagram showing the forces acting on the device in the case in which the radius $R_s > 2\ell$ of the solenoid is sufficiently large to fully host the device and its motion (Case I). Four scenarios are depicted: (a) the device is in the static equilibrium configuration determined in Equation (43); (b) although the device is in a configuration with initial null velocities, such configuration is not of equilibrium because the Lorentz force, composed only by its electric contribution, produces a non-zero torque, thereby triggering the motion; (c and d) in each case the device is in a deformed configuration with nonzero velocities and, thus, the magnetic part of the Lorentz force acts on the device in addition to the electric part. In particular, we emphasize that, while $\mathfrak{e}\,\boldsymbol{v}_D \times \boldsymbol{B}$ is parallel to $\boldsymbol{n}_2$ by construction, $\mathfrak{e}\boldsymbol{E}$ has to be tangential to the circumference instantaneously centered in the origin and passing through $x_D(t)$ (indeed, $\boldsymbol{E}(x_D(t), t)$ is proportional to $\boldsymbol{e}_3 \times \boldsymbol{r}(x_D(t))$, with $\boldsymbol{r}(x_D(t)) = x_{D1}(t)\,\boldsymbol{e}_1 + x_{D2}(t)\,\boldsymbol{e}_2$).

Before proceeding with the stability analysis, we notice that Equations (34a)–(34c) feature together six physical parameters to which we add the magnitude F of the dead load applied to the cart and the $\boldsymbol{e}_3$-component $B_h(t)$ of the magnetic induction field:

$$\mathcal{P} := \{m_c;\ m, c, k, \ell;\ \mathfrak{e};\ F, B_M\}, \tag{44}$$

with $B_M := \max_t |B_h(t)|$.

Dimensionless quantities are introduced via the mappings

$$X_c \mapsto \frac{X_c}{\ell}, \qquad t \mapsto \frac{t}{\sqrt{m\ell^2/k}}, \qquad \mu \mapsto \frac{\mu\ell}{k}, \qquad F \mapsto \frac{F\ell}{k}, \qquad B_M \mapsto \frac{\mathfrak{e}B_M\ell}{\sqrt{mk}}, \tag{45a}$$

$$M \mapsto \frac{M}{m}, \qquad c \mapsto \frac{c}{\ell\sqrt{mk}}. \tag{45b}$$

For simplicity, we do not introduce additional notation to indicate the dimensionless quantities in Equations (45a) and (45b). Rather, from here on, we simply rename them as X_c, t, μ, F, B_M, M, and c, and we differentiate with respect to the dimensionless time variable. We emphasize that dimensionless variables are used throughout Section 4, and physical dimensions are restored in Section 5 to contextualize the numerical results.

4.1. Linearization of the equations governing the dynamics of the structure

To perform the stability analysis in a neighborhood of the pair $(q_e; \mu_e) = (0, 0, -2; F)$, we consider small *perturbations* around q_e and μ_e. This is achieved by introducing the homotopies

$\tilde{q}$ and $\tilde{\mu}$, which define the perturbed configuration $\tilde{q}(t,\varepsilon)$ and the perturbed Lagrange multiplier $\tilde{\mu}(t,\varepsilon)$, with ε being a smallness parameter, and by requiring them to comply with the conditions $\tilde{q}(t,0) = q_\mathrm{e}$ and $\tilde{\mu}(t,0) = \mu_\mathrm{e}$. We assume $\tilde{q}$ and $\tilde{\mu}$ to be at least C^2 functions of their arguments.

The first-order expansions of $\tilde{q}$ and $\tilde{\mu}$ around $\varepsilon = 0$ and for all t can be written as:

$$\tilde{q}(t,\varepsilon) = q_\mathrm{e} + \eta(t)\varepsilon + o(\varepsilon), \quad \varepsilon \to 0, \tag{46a}$$

$$\tilde{\mu}(t,\varepsilon) = \mu_\mathrm{e} + \varrho(t)\varepsilon + o(\varepsilon), \quad \varepsilon \to 0, \tag{46b}$$

with $\eta(t) \coloneqq \partial_\varepsilon \tilde{q}(t,0)$ and $\varrho(t) \coloneqq \partial_\varepsilon \tilde{\mu}(t,0)$. In the following, we set $\eta \coloneqq (\vartheta_1, \vartheta_2, x_\mathrm{c})$.

By substituting Equations (46a) and (46b) into the dimensionless form of Equations (34a)–(34c) and (36), and dropping all terms of order higher than the first in ε, we obtain the dynamic equations linearized around q_e and μ_e:

$$\tfrac{5}{4}\ddot{\vartheta}_1 + \tfrac{1}{2}\ddot{\vartheta}_2 + c\,(2\dot{\vartheta}_1 - \dot{\vartheta}_2) + (2\vartheta_1 - \vartheta_2) - F(\vartheta_1 - \vartheta_2) + B_\mathrm{h}(t)\dot{x}_\mathrm{c} + \tfrac{1}{2}\dot{B}_\mathrm{h}(t)x_\mathrm{c} = 0, \tag{47a}$$

$$\tfrac{1}{2}\ddot{\vartheta}_1 + \tfrac{1}{4}\ddot{\vartheta}_2 + c\,(\dot{\vartheta}_2 - \dot{\vartheta}_1) + (\vartheta_2 - \vartheta_1) + B_\mathrm{h}(t)\dot{x}_\mathrm{c} + \tfrac{1}{2}\dot{B}_\mathrm{h}(t)x_\mathrm{c} = 0, \tag{47b}$$

$$M\ddot{x}_\mathrm{c} + \varrho - B_\mathrm{h}(t)(\dot{\vartheta}_1 + \dot{\vartheta}_2) - \tfrac{1}{2}\dot{B}_\mathrm{h}(t)(\vartheta_1 + \vartheta_2) = 0, \tag{47c}$$

$$\ddot{x}_\mathrm{c} = 0, \tag{47d}$$

where $B_\mathrm{h}(t)$ and $\dot{B}_\mathrm{h}(t)$ are dimensionless functions of dimensionless time. Accordingly, the dimensionless characteristic amplitude B_M of the magnetic induction field, as shown in Equation $(45\mathrm{a})_5$, is understood as $\max_t |B_\mathrm{h}(t)| = B_\mathrm{M}$.

Remark 3 (Lorentz force couples the translational and the rotational degrees of freedom)**.** *In the linearized dynamic equations* (47a)–(47c)*, $B_\mathrm{h}(t)$ and $\dot{B}_\mathrm{h}(t)$ make it impossible to decouple x_c from ϑ_1 and ϑ_2. This holds true even in the case in which the condition $\dot{x}_\mathrm{c} = 0$ (representing the linearization of the constraint* (4)*) is substituted in* (47a)–(47c)*, because the terms involving $\dot{B}_\mathrm{h}(t)$ do not cancel, as they represent the electric part of the Lorentz force. This is another difference with the case studied by Cazzolli et al. [3] in which the absence of the Lorentz force allows for decoupling the dynamics of the cart from the dynamics of the double pendulum.*

Following Neimark and Fufaev [23], upon introducing the 3×1 array $\mathsf{\eta} = \{\vartheta_1\ \vartheta_2\ x_\mathrm{c}\}^\mathrm{T}$ and the 1×1 array $\mathsf{\rho} = \{\varrho\}$, Equations (47a)–(47d) can be recast in matrix formalism as

$$\mathsf{M}_\mathrm{e}\ddot{\mathsf{\eta}} + [\mathsf{C}_\mathrm{e} + B_\mathrm{h}\mathsf{L}_\mathrm{e}]\,\dot{\mathsf{\eta}} + [\mathsf{K}_\mathrm{e} + F\mathsf{G}_\mathrm{e} + \tfrac{1}{2}\dot{B}_\mathrm{h}\mathsf{L}_\mathrm{e}]\,\mathsf{\eta} - \mathsf{A}_\mathrm{e}^\mathrm{T}\mathsf{\rho} = \mathsf{0}, \tag{48a}$$

$$-\mathsf{A}_\mathrm{e}\,\ddot{\mathsf{\eta}} = \mathsf{0}, \tag{48b}$$

where M_e, K_e, and C_e represent the mass, stiffness, and damping matrices, respectively, G_e is an auxiliary (singular) matrix introduced to account for the force F, A_e is the constraint matrix, while L_e is the matrix accounting for the contributions due to the Lorentz force. These matrices read

$$\mathsf{M}_\mathrm{e} \coloneqq \begin{bmatrix} \frac{5}{4} & \frac{1}{2} & 0 \\ \frac{1}{2} & \frac{1}{4} & 0 \\ 0 & 0 & M \end{bmatrix}, \qquad \mathsf{K}_\mathrm{e} \coloneqq \begin{bmatrix} 2 & -1 & 0 \\ -1 & 1 & 0 \\ 0 & 0 & 0 \end{bmatrix}, \qquad \mathsf{C}_\mathrm{e} \coloneqq \begin{bmatrix} 2c & -c & 0 \\ -c & c & 0 \\ 0 & 0 & 0 \end{bmatrix}, \tag{49a}$$

$$\mathsf{G}_\mathrm{e} \coloneqq \begin{bmatrix} -1 & 1 & 0 \\ 0 & 0 & 0 \\ 0 & 0 & 0 \end{bmatrix}, \qquad \mathsf{A}_\mathrm{e} \coloneqq \begin{bmatrix} 0 & 0 & -1 \end{bmatrix}, \qquad \mathsf{L}_\mathrm{e} \coloneqq \begin{bmatrix} 0 & 0 & 1 \\ 0 & 0 & 1 \\ -1 & -1 & 0 \end{bmatrix}. \tag{49b}$$

Remark 4 (Faraday tensor in matrix formalism and its coupling with C_e, K_e, and $F\mathsf{G}_\mathrm{e}$)**.** *In the linearized setting, the dead load F, although being applied to the cart, influences the double pendulum through the introduction of the 'apparent' stiffness matrix $F\mathsf{G}_\mathrm{e}$, referred to as* 'geometric stiffness matrix' *in the literature [10] and adding to the elastic stiffness matrix K_e. Similarly, B_h and $\dot{B}_\mathrm{h}$ yield the 'apparent' damping matrix $B_\mathrm{h}\mathsf{L}_\mathrm{e}$ and the additional 'apparent' stiffness matrix $\frac{1}{2}\dot{B}_\mathrm{h}\mathsf{L}_\mathrm{e}$, both due to the linearization of the Lorentz force. It is worth noticing that $B_\mathrm{h}\mathsf{L}_\mathrm{e}$ is the matrix associated with the generalized Faraday tensor, evaluated at the equilibrium configuration q_e in dimensionless form and in the case in which the device is inside the solenoid (cfr. Equation* (30a)*). Analogously, $\frac{1}{2}\dot{B}_\mathrm{h}\mathsf{L}_\mathrm{e}$ is the matrix associated with the electric contribution $\frac{1}{2}\dot{B}_\mathrm{h}\mathsf{L}_\mathrm{e}\eta$ of the Lorentz force. We emphasize that the terms $B_\mathrm{h}\mathsf{L}_\mathrm{e}$ and $\frac{1}{2}\dot{B}_\mathrm{h}\mathsf{L}_\mathrm{e}$ constitute another relevant difference from the work by Cazzolli et al. [3] and add to the damping matrix C_e and to the stiffness matrix K_e, respectively.*

To solve Equation (48a) and (48b), we follow standard methods [23], and we enforce the *ansatz*

$$\eta(t) = \mathsf{H}\,\mathrm{e}^{\lambda t}, \quad \rho(t) = \mathsf{R}\,\mathrm{e}^{\lambda t}, \qquad \lambda \in \mathbb{C}, \tag{50}$$

where H and R are two column vectors of constant amplitudes, having sizes 3×1 and 1×1, respectively, and λ is a complex number. Substituting Equation (50) into (48a) and (48b) yields

$$\left[\begin{array}{c|c} \lambda^2\mathsf{M}_\mathrm{e} + \lambda[\mathsf{C}_\mathrm{e} + B_\mathrm{h}\mathsf{L}_\mathrm{e}] + [\mathsf{K}_\mathrm{e} + F\mathsf{G}_\mathrm{e} + \frac{1}{2}\dot{B}_\mathrm{h}\mathsf{L}_\mathrm{e}] & -\mathsf{A}_\mathrm{e}^\mathrm{T} \\ \hline -\lambda^2\mathsf{A}_\mathrm{e} & 0 \end{array}\right] \begin{Bmatrix} \mathsf{H} \\ \mathsf{R} \end{Bmatrix} = \begin{Bmatrix} 0 \\ 0 \end{Bmatrix}, \tag{51}$$

where 0 denotes here the 3×1 null array.

To find nontrivial solutions to Equation (51), we impose that the determinant of the block-wise matrix on the left-hand side of Equation (51) vanish. Before proceeding, we remark that the term $\lambda^2\mathsf{A}_\mathrm{e}$ in the block-wise matrix of Equation (51) would lead to a sixth-grade characteristic polynomial in λ featuring a factor λ^2. This corresponds to a vanishing root of algebraic multiplicity two, which, as explained by Neimark and Fufaev [23, p. 265–267], does not affect the overall stability properties of the system. Hence, we introduce the alternative system

$$\left[\begin{array}{c|c} \lambda^2\mathsf{M}_\mathrm{e} + \lambda[\mathsf{C}_\mathrm{e} + B_\mathrm{h}\mathsf{L}_\mathrm{e}] + [\mathsf{K}_\mathrm{e} + F\mathsf{G}_\mathrm{e} + \frac{1}{2}\dot{B}_\mathrm{h}\mathsf{L}_\mathrm{e}] & -\mathsf{A}_\mathrm{e}^\mathrm{T} \\ \hline -\mathsf{A}_\mathrm{e} & 0 \end{array}\right] \begin{Bmatrix} \mathsf{H} \\ \mathsf{R} \end{Bmatrix} = \begin{Bmatrix} 0 \\ 0 \end{Bmatrix}. \tag{52}$$

Computing the determinant of the block-wise matrix on the left-hand side of Equation (52) yields a polynomial equation of the fourth-grade in λ, which can be written as

$$Q(\lambda) \coloneqq a_0\lambda^4 + a_1\lambda^3 + a_2\lambda^2 + a_3\lambda + a_4 = 0, \tag{53}$$

with the coefficients a_0, a_1, a_2, a_3, a_4 being all real and given by

$$a_0 = 1, \qquad a_1 = 44\,c, \qquad a_2 = 44 + 16\,c^2 - 12F, \qquad a_3 = 32\,c, \qquad a_4 = 16. \tag{54}$$

An important result unfolded by the coefficients $a_0, \ldots, a_4$ is that, in spite of the Lorentz force contributions to Equation (52), the characteristic polynomial (53) depends neither on $B_\mathrm{h}(t)$ nor on $\dot{B}_\mathrm{h}(t)$. To see why this result holds true from the algebraic point of view, we report in Figure 4 a sketch of the structure of the block-wise matrix in Equation (52) and of the calculation of its

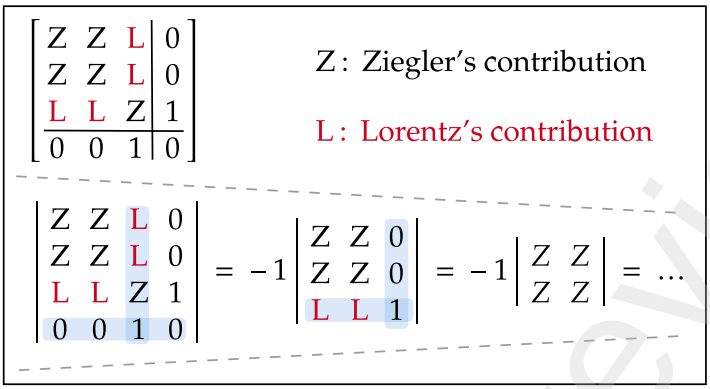

Figure 4: Sketch of the proof that the determinant of the block-wise matrix on the left-hand side of Equation (52) depends neither on $B_{\mathrm{h}}(t)$ nor on $\dot{B}_{\mathrm{h}}(t)$.

determinant. Thus, the linear stability analysis falls back to that of Ziegler's double pendulum [3, 6, 10].

Although a_0 is equal to unity, a_1 and a_3 depend only on c, and a_2 depends on both c and F, it is convenient to regard all coefficients as *formally* depending on c and F. In particular, as the purpose of this study is to analyze the stability of the system under the dead load F, the coefficients $a_0, a_1, \ldots, a_4$ are regarded as functions of F, parameterized by c.

The polynomial equation (53) has in general four complex roots. Since it has real coefficients and is of even grade, its four roots, hereafter denoted as $\lambda_1, \lambda_2, \lambda_3, \lambda_4$, are paired in the sense that, if λ_1 and λ_2 are complex numbers, then $\lambda_4 \equiv \bar{\lambda}_1$ and $\lambda_3 \equiv \bar{\lambda}_2$. We also notice that the roots $\lambda_1, \lambda_2, \lambda_3, \lambda_4$ are functions of F depending parametrically on c.

4.1.1. The case of the undamped double pendulum: symmetric diagram of the roots

If c is set equal to zero, Equation (53) simplifies to a biquadratic equation in λ, since the coefficients a_1 and a_3 disappear. Hence, by setting $\Delta(F) := [a_2(F)]^2 - 4a_4(F)$, the roots of Equation (53) can be solved for λ^2 as

$$\lambda_1^2(F) = -\frac{a_2(F)}{2} - \frac{\sqrt{\Delta(F)}}{2}, \qquad \lambda_2^2(F) = -\frac{a_2(F)}{2} + \frac{\sqrt{\Delta(F)}}{2}, \qquad \text{if } \Delta(F) \geq 0, \tag{55a}$$

$$\lambda_1^2(F) = -\frac{a_2(F)}{2} - i\frac{\sqrt{|\Delta(F)|}}{2}, \qquad \lambda_2^2(F) = -\frac{a_2(F)}{2} + i\frac{\sqrt{|\Delta(F)|}}{2}, \qquad \text{if } \Delta(F) < 0. \tag{55b}$$

Note that the form of $\lambda_1^2(F)$ and $\lambda_2^2(F)$ in Equations (55a) and (55b) depends on the asymmetry of the matrix $\mathsf{K}_{\mathrm{e}} + F\mathsf{G}_{\mathrm{e}}$ when $F \neq 0$. Indeed, when this matrix is symmetric, the roots λ are purely imaginary [10].

For the following calculations, it is convenient to introduce the auxiliary quantities

$$H_1(F) := \frac{a_2(F)}{2} + \frac{\sqrt{\Delta(F)}}{2}, \qquad H_2(F) := \frac{a_2(F)}{2} - \frac{\sqrt{\Delta(F)}}{2}, \qquad \text{if } \Delta(F) \geq 0, \tag{56a}$$

$$K_1(F) := \frac{a_2(F)}{2} + i\frac{\sqrt{|\Delta(F)|}}{2}, \qquad K_2(F) := \frac{a_2(F)}{2} - i\frac{\sqrt{|\Delta(F)|}}{2}, \qquad \text{if } \Delta(F) < 0. \tag{56b}$$

For notational convenience, we set $K(F) := K_1(F) \equiv \bar{K}_2(F)$ for $\Delta(F) < 0$.

Case #1: $\Delta = 0$. We have $H_1(F) \equiv H_2(F) \equiv H(F) \coloneqq a_2(F)/2$, and, in terms of the values assumed by a_2 and a_4, the discriminant $\Delta \coloneqq a_2^2 - 4a_4$ vanishes at the two *critical* values of F:

$$F_1 = 3, \qquad F_2 = \frac{13}{3}. \tag{57}$$

For these values, the squared eigenvalues are

$$\lambda_1^2(F_1) = \lambda_2^2(F_1) = -H(F_1) = -\frac{a_2(F_1)}{2} = -4 = i^2 4, \tag{58}$$

$$\lambda_1^2(F_2) = \lambda_2^2(F_2) = -H(F_2) = -\frac{a_2(F_2)}{2} = +4, \tag{59}$$

leading to

$$\lambda_{1,1}(F_1) = \lambda_{2,1}(F_1) = -i2, \qquad \lambda_{1,2}(F_1) = \lambda_{2,2}(F_1) = +i2, \tag{60a}$$

$$\lambda_{1,2}(F_2) = \lambda_{2,1}(F_2) = -2, \qquad \lambda_{1,1}(F_2) = \lambda_{2,2}(F_2) = +2. \tag{60b}$$

Case #2: $\Delta > 0$. The discriminant Δ is positive for the values of F:

$$F \in [0, F_1\,[\cup]F_2, +\infty[. \tag{61}$$

Two situations occur:

2.1 For $F \in [0, F_1[$, the coefficient $a_2(F)$ is strictly positive. The following two different *real* and *negative* values of λ^2 exist

$$0 > \lambda_1^2(F) = i^2 H_1(F), \qquad H_1(F) > 0, \tag{62a}$$

$$0 > \lambda_2^2(F) = i^2 H_2(F), \qquad H_2(F) > 0. \tag{62b}$$

Since $\lambda_1^2(F)$ and $\lambda_2^2(F)$ are negative, each of them produces a pair of purely imaginary conjugate roots,

$$\lambda_{1,1}(F) = -i\sqrt{H_1(F)}, \qquad \lambda_{1,2}(F) = +i\sqrt{H_1(F)}, \tag{63a}$$

$$\lambda_{2,1}(F) = -i\sqrt{H_2(F)}, \qquad \lambda_{2,2}(F) = +i\sqrt{H_2(F)}. \tag{63b}$$

Accordingly, the system linearized about the static equilibrium is *marginally stable* [29]. So, if perturbed from equilibrium, the system oscillates around its equilibrium configuration. We emphasize that the necessary and sufficient condition for stability, which requires the real part of all the roots to be strictly negative [29], is not met in this first case.

2.2 For $F \in]F_2, +\infty[$, the coefficient $a_2(F)$ is strictly negative and the following two *real* and *positive* values for λ^2 exist

$$0 < \lambda_1^2(F) = -H_1(F), \qquad H_1(F) < 0, \tag{64a}$$

$$0 < \lambda_2^2(F) = -H_2(F), \qquad H_2(F) < 0, \tag{64b}$$

each of which produces one pair of real roots,

$$\lambda_{1,1}(F) = +\sqrt{-H_1(F)}, \qquad \lambda_{1,2}(F) = -\sqrt{-H_1(F)}, \tag{65a}$$

$$\lambda_{2,1}(F) = -\sqrt{-H_2(F)}, \qquad \lambda_{2,2}(F) = +\sqrt{-H_2(F)}. \tag{65b}$$

Since $\lambda_{1,1}(F)$ and $\lambda_{2,2}(F)$ are real and strictly positive for $F \in]F_2, +\infty[$, the phenomenon of 'blow up', or divergence, is expected to occur in this range of values of F, where the solution is *not* oscillatory.

Case #3: $\Delta < 0$. The discriminant Δ is negative for the following values of F:

$$F \in]F_1, F_2[. \tag{66}$$

Two *complex conjugate* values for λ^2 exist,

$$\lambda_1^2(F) = -K_1(F) = -K(F), \tag{67a}$$

$$\lambda_2^2(F) = -K_2(F) = -\bar{K}(F), \tag{67b}$$

whose roots are given by

$$\lambda_{1,1}(F) = -i\sqrt{\rho(F)}\exp\left(+i\frac{\phi(F)}{2}\right), \qquad \lambda_{1,2}(F) = +i\sqrt{\rho(F)}\exp\left(+i\frac{\phi(F)}{2}\right), \tag{68a}$$

$$\lambda_{2,1}(F) = -i\sqrt{\rho(F)}\exp\left(-i\frac{\phi(F)}{2}\right), \qquad \lambda_{2,2}(F) = +i\sqrt{\rho(F)}\exp\left(-i\frac{\phi(F)}{2}\right). \tag{68b}$$

where

$$\rho(F) \coloneqq \sqrt{\mathrm{Re}[K(F)]^2 + \mathrm{Im}[K(F)]^2}, \qquad \phi(F) \coloneqq \arctan\left(\frac{\mathrm{Im}[K(F)]}{\mathrm{Re}[K(F)]}\right). \tag{69}$$

Note that the following conjugacy relations hold: $\lambda_{1,1}(F) = \bar{\lambda}_{2,2}(F)$ and $\lambda_{1,2}(F) = \bar{\lambda}_{2,1}(F)$.

For future reference, we also provide for these roots the equivalent expressions

$$\lambda_{1,1}(F) = \sqrt{\rho(F)}\left(+\sin\frac{\phi(F)}{2} - i\cos\frac{\phi(F)}{2}\right), \qquad \lambda_{1,2}(F) = \sqrt{\rho(F)}\left(-\sin\frac{\phi(F)}{2} + i\cos\frac{\phi(F)}{2}\right), \tag{70a}$$

$$\lambda_{2,1}(F) = \sqrt{\rho(F)}\left(-\sin\frac{\phi(F)}{2} - i\cos\frac{\phi(F)}{2}\right), \qquad \lambda_{2,2}(F) = \sqrt{\rho(F)}\left(+\sin\frac{\phi(F)}{2} + i\cos\frac{\phi(F)}{2}\right). \tag{70b}$$

Referring to Figure 5a, since the real parts $\mathrm{Re}[\lambda_{1,2}(F)] = \mathrm{Re}[\lambda_{2,1}(F)] < 0$ are negative for all the considered values of $F \in]F_1, F_2[$, the roots $\lambda_{1,2}(F)$ and $\lambda_{2,1}(F)$ yield oscillating solutions with amplitude decreasing to zero as time increases. However, since the real parts $\mathrm{Re}[\lambda_{1,1}(F)] = \mathrm{Re}[\lambda_{2,2}(F)]$ are positive, the roots $\lambda_{1,1}(F)$ and $\lambda_{2,2}(F)$ yield oscillating solutions with amplitudes increasing in time, thereby being responsible for the globally unstable behavior of the system. This phenomenon is known as *flutter instability* [10].

With these cases in mind, the critical values F_1 and F_2 henceforth will be renamed $F_{\mathrm{flu}}^{\mathrm{nd}}$ and $F_{\mathrm{div}}^{\mathrm{nd}}$ to indicate that they specify, in the absence of damping (superscript 'nd'), the values of F delimitating the region of flutter. In particular, for $F > F_{\mathrm{flu}}^{\mathrm{nd}}$ at least one root has positive real part, and, thus, the system passes from the marginally stable region to the first unstable region in which flutter occurs. The second critical value $F_{\mathrm{div}}^{\mathrm{nd}} > F_{\mathrm{flu}}^{\mathrm{nd}}$ marks the end of the flutter regime, and, for $F > F_{\mathrm{div}}^{\mathrm{nd}}$, the region of divergence instability, without oscillatory behavior. It is worth emphasizing that, at $F_{\mathrm{flu}}^{\mathrm{nd}}$ and $F_{\mathrm{div}}^{\mathrm{nd}}$, the real parts of the roots split into different branches, whereas the imaginary parts coalesce. This is illustrated in Figure 5a, where the points B_0, B_1, and B_2 highlight the three branching points of the real parts when $c = 0$.

From now on, we adopt the following numbering of the roots, which ensures that both the real and imaginary parts of all roots are continuous functions of F, while preserving pairwise conjugacy (i.e., $\lambda_1(F)$ and $\lambda_4(F)$ are complex conjugate, and $\lambda_2(F)$ and $\lambda_3(F)$ are complex conjugate for $F \in [0, F_{\mathrm{div}}^{\mathrm{nd}}]$):

$$\lambda_1(F) = \begin{cases} \lambda_{1,2}(F) & \text{if } F \in [0, F_{\mathrm{flu}}^{\mathrm{nd}}[\,, \\ \lambda_{1,2}(F) & \text{if } F \in [F_{\mathrm{flu}}^{\mathrm{nd}}, F_{\mathrm{div}}^{\mathrm{nd}}], \\ \lambda_{2,1}(F) & \text{if } F \in]F_{\mathrm{div}}^{\mathrm{nd}}, +\infty[\,. \end{cases} \qquad \lambda_2(F) = \begin{cases} \lambda_{2,2}(F) & \text{if } F \in [0, F_{\mathrm{flu}}^{\mathrm{nd}}[\,, \\ \lambda_{2,2}(F) & \text{if } F \in [F_{\mathrm{flu}}^{\mathrm{nd}}, F_{\mathrm{div}}^{\mathrm{nd}}], \\ \lambda_{2,2}(F) & \text{if } F \in]F_{\mathrm{div}}^{\mathrm{nd}}, +\infty[\,. \end{cases} \tag{71a}$$

$$\lambda_3(F) = \begin{cases} \lambda_{2,1}(F) & \text{if } F \in [0, F^{\mathrm{nd}}_{\mathrm{flu}}[\,, \\ \lambda_{1,1}(F) & \text{if } F \in [F^{\mathrm{nd}}_{\mathrm{flu}}, F^{\mathrm{nd}}_{\mathrm{div}}], \\ \lambda_{1,1}(F) & \text{if } F \in]F^{\mathrm{nd}}_{\mathrm{div}}, +\infty[\,. \end{cases} \qquad \lambda_4(F) = \begin{cases} \lambda_{1,1}(F) & \text{if } F \in [0, F^{\mathrm{nd}}_{\mathrm{flu}}[\,, \\ \lambda_{2,1}(F) & \text{if } F \in [F^{\mathrm{nd}}_{\mathrm{flu}}, F^{\mathrm{nd}}_{\mathrm{div}}], \\ \lambda_{1,2}(F) & \text{if } F \in]F^{\mathrm{nd}}_{\mathrm{div}}, +\infty[\,. \end{cases} \tag{71b}$$

4.1.2. The case of the damped double pendulum: asymmetric diagram of the roots

In this section the critical loads of flutter and divergence are obtained for $c > 0$. Two different techniques are used, one to determine the critical load for flutter and another to derive the critical load for divergence, which are now explicitly regarded as depending on c, as indicated by the notation $F_{\mathrm{flu}}(c)$ and $F_{\mathrm{div}}(c)$. The first method is the Routh–Hurwitz stability criterion [6, 29] and provides an explicit expression for $F_{\mathrm{flu}}(c)$. The second method relies on the direct inspection of the characteristic polynomial provided in Equation (53), whereby we compute numerically $F_{\mathrm{div}}(c)$ for given values of $c > 0$.

Critical load for flutter. The Routh–Hurwitz criterion is a direct test done on the coefficients of a polynomial to determine if all of its roots lie on the left half of the complex plane, i.e., if they all have negative real parts. This criterion is applied to the characteristic equation (53), to determine necessary and sufficient conditions on F that guarantee that the roots $\lambda_1, \lambda_2, \lambda_3, \lambda_4$ all have negative real parts. This yields the threshold value, $F_{\mathrm{flu}}(c)$, approached from the left, i.e., in the limit $F \to [F_{\mathrm{flu}}(c)]^-$, with the force range $[0, F_{\mathrm{flu}}(c)[$ corresponding to the region, in the undamped case, in which all the roots have zero real part, see Figure 5a for $F \in [0, F^{\mathrm{nd}}_{\mathrm{flu}}[$.

The Hurwitz matrix associated with the characteristic polynomial in (53) is

$$\mathsf{H}_4 = \begin{bmatrix} a_1 & a_0 & 0 & 0 \\ a_3 & a_2 & a_1 & a_0 \\ 0 & a_4 & a_3 & a_2 \\ 0 & 0 & 0 & a_4 \end{bmatrix}. \tag{72}$$

Considering now all the principle minors which are generated by H_4, the condition to guarantee stability of the system is that *all* of these principle minors must be strictly positive, leading to the following stability conditions:

$$0 < a_1, \tag{73a}$$
$$0 < a_1 a_2 - a_0 a_3, \tag{73b}$$
$$0 < a_3(a_1 a_2 - a_0 a_3) - a_1^2 a_4, \tag{73c}$$
$$0 < (a_3(a_1 a_2 - a_0 a_3) - a_1^2 a_4) a_4. \tag{73d}$$

Since $a_1 = 44c$ (see Equation $(54)_2$), the inequality (73a) is identically satisfied for positive damping coefficients. Moreover, the condition (73d) coincides with Equation (73c) multiplied by a_4, which is positive (see Equation $(54)_4$, in which $a_4 = 16$). Hence, the inequality (73d) is satisfied automatically if the condition (73c) is fulfilled. Therefore, only inequalities (73b) and (73c) have to be considered. Their solution leads to the threshold value for F, $F_{\mathrm{flu}}(c)$, below which all the roots have negative real part. Such condition reads [10]

$$F < F_{\mathrm{flu}}(c), \qquad F_{\mathrm{flu}}(c) = \frac{39}{22} + \frac{4c^2}{3}. \tag{74}$$

Therefore, the system is stable for $F < F_{\mathrm{flu}}(c)$, and it experiences flutter or divergence instability otherwise. More in detail, $F_{\mathrm{flu}}(c)$ defines, for varying damping coefficient $c > 0$, the onset of *flutter* when damping is present.

Critical load for divergence. The critical load for divergence is obtained by directly examining the discriminant of the characteristic polynomial (53). The general formula for the discriminant of a polynomial $Q(\lambda)$ of grade n is given in [30] as

$$D[Q] = (-1)^{n(n-1)/2} a_0^{-1} \mathrm{Res}[Q, Q'], \qquad Q(\lambda) = a_0\lambda^n + a_1\lambda^{n-1} + \cdots + a_{n-1}\lambda + a_n, \tag{75}$$

where $Q'(\lambda)$ is the derivative of $Q(\lambda)$ with respect to λ, and $\mathrm{Res}[Q, Q']$ is the 'resultant' of the polynomials $Q(\lambda)$ and $Q'(\lambda)$. Since the grade n is equal to 4, $\mathrm{Res}[Q, Q']$ can be computed as the determinant of the Sylvester matrix $\mathsf{S}_n \equiv \mathsf{S}_4$ formed by the polynomials $Q(\lambda)$ and $Q'(\lambda)$ [31, 32],

$$\mathrm{Res}[Q, Q'] \coloneqq \det(\mathsf{S}_4) = \begin{vmatrix} a_0 & a_1 & a_2 & a_3 & a_4 & 0 & 0 \\ 0 & a_0 & a_1 & a_2 & a_3 & a_4 & 0 \\ 0 & 0 & a_0 & a_1 & a_2 & a_3 & a_4 \\ 4a_0 & 3a_1 & 2a_2 & a_3 & 0 & 0 & 0 \\ 0 & 4a_0 & 3a_1 & 2a_2 & a_3 & 0 & 0 \\ 0 & 0 & 4a_0 & 3a_1 & 2a_2 & a_3 & 0 \\ 0 & 0 & 0 & 4a_0 & 3a_1 & 2a_2 & a_3 \end{vmatrix}. \tag{76}$$

Note that, in our case, $a_0 = 1$. We emphasize that, for $c \neq 0$, the general formula $D[Q]$ must be used because, although $n = 4$, the polynomial $Q(\lambda)$ no longer reduces to a quadratic polynomial in λ^2, as it does for $c = 0$. Thus, Equation $(75)_1$ becomes

$$\begin{aligned} D[Q] = {} & 256a_4^3 - 192a_1a_3a_4^2 - 128a_2^2a_4^2 + 144a_2a_3^2a_4 - 27a_3^4 + 144a_1^2a_2a_4^2 \\ & - 6a_1^2a_3^2a_4 - 80a_1a_2^2a_3a_4 + 18a_1a_2a_3^3 + 16a_2^4a_4 - 4a_2^3a_3^2 \\ & - 27a_1^4a_4^2 + 18a_1^3a_2a_3a_4 - 4a_1^3a_3^3 - 4a_1^2a_2^3a_4 + a_1^2a_2^2a_3^2. \end{aligned} \tag{77}$$

Since a_1, a_2, a_3, and a_4 can be formally regarded as functions of F—although, in fact, only a_2 depends on F (see Equation (54))—we may write $D[Q] \equiv P(F)$, where $P(F)$ is a quartic polynomial in F whose coefficients depend parametrically on $c > 0$. The expression for $P(F)$ is too lengthy to be reported here. However, the equation $P(F) = 0$ is solved numerically to determine the values of F that, for fixed $c > 0$, cause the discriminant (77) to vanish. In correspondence of these values of F, the nature of the roots $\lambda_1, \lambda_2, \lambda_3, \lambda_4$ of $Q(\lambda)$ changes. Specifically, two of the four solutions to $P(F) = 0$ are complex conjugate, and can be disregarded, because the force F should be represented by real numbers only. The two remaining solutions are real numbers corresponding to the branching points of the real parts of the roots of $Q(\lambda)$ in Equation (53), represented by points B_1 and B_2 in Figure 5b. In Figure 5b, corresponding to the case $c = 0.1$, the larger of the two real solutions identifies the branching point B_2. For values of F above this threshold, all the roots of $Q(\lambda)$ have zero imaginary part. In particular, two of them have a negative real part, and the other two have a positive real part, which leads to blow-up, or divergence (without oscillations), of the solutions ϑ_1 and ϑ_2 of the double pendulum.

By using the Routh–Hurwitz criterion, Equation (74), and determining the zeros of $P(F)$ for $c = 0.1$, the threshold values for F are found

$$F_{\mathrm{flu}}(c = 0.1) = 1.7861, \qquad F_{\mathrm{div}}(c = 0.1) = 5.1623, \tag{78}$$

corresponding to the onset of the flutter and divergence instabilities, respectively, in the presence of damping. The λ-F diagram for $c = 0.1$ is presented in Figure 5b.

Remark 5 (Ziegler's paradox [8, 9, 10])**.** *If one assumes $c = 0$, the results presented in Section 4.1.1 must be recovered. Indeed, one obtains $D[Q] \equiv P(F) \equiv 16\, a_4(F)[\Delta(F)]^2$ and, thus, the vanishing of $P(F)$ yields the two real and positive values $F = F^{\mathrm{nd}}_{\mathrm{flu}} = 3$ and $F = F^{\mathrm{nd}}_{\mathrm{div}} = 13/3$, but both with multiplicity two. In this case, in which c is set equal to zero, there are no dissipative mechanisms in the double pendulum subsystem that can produce limit cycles in the fluttering regime. However,* Ziegler's paradox *[8, 9, 10] consists precisely in the fact that $F^{\mathrm{nd}}_{\mathrm{flu}} = 3$ exceeds the infimum of $F_{\mathrm{flu}}(c)$ for $c \in]0, +\infty[$, as computed via the Routh–Hurwitz criterion in Equation* (74)*,*

$$F^{\mathrm{nd}}_{\mathrm{flu}} = 3 > F^{(0)}_{\mathrm{flu}} \coloneqq \lim_{c \to 0^+} F_{\mathrm{flu}}(c) = 39/22 \simeq 1.7727. \tag{79}$$

Thus, for $F \in]F^{(0)}_{\mathrm{flu}}, F^{\mathrm{nd}}_{\mathrm{flu}}]$, the roots of $Q(\lambda)$ may take on non-negative values. Hence, one may find damping coefficients $c > 0$ such that for F compliant with $F^{(0)}_{\mathrm{flu}} < F_{\mathrm{flu}}(c) \leq F \leq F^{\mathrm{nd}}_{\mathrm{flu}}$, the roots of $Q(\lambda)$ can have non-negative real part and non-zero imaginary part, so that flutter occurs.

Remark 6 (Symmetry breaking of the λ-F diagram due to the presence of damping)**.** *It is of interest to examine how the branching and merging points of the real and imaginary parts of the roots of $Q(\lambda)$ change from Figure 5a to Figure 5b when switching from null damping to nonzero damping (in this case, $c = 0.1$). Specifically, the value $F = F^{\mathrm{nd}}_{\mathrm{flu}} = 3$ corresponds to the branching point B_0 in the λ-F diagram in the case without damping, Figure 5a, whereas branching does not occurs at $F = F_{\mathrm{flu}}(c = 0.1)$, when damping is present, as shown in Figure 5b (point H in the magnified region). The beginning of the flutter instability depends only on whether the load F exceeds the critical value $F_{\mathrm{flu}}(c = 0.1)$, not on the presence of a branching point in the λ-F diagram. Moreover, in the damped case the real parts of the roots $\lambda_1(F)$ (solid line marked with diamond) and $\lambda_4(F)$ (solid line marked with circles) overlap from $F = 0$ until the value of F corresponding to B_1. The same applies also to $\lambda_2(F)$ (solid line marked with triangles) and $\lambda_3(F)$ (solid line marked with squares) from $F = 0$ until the value of F corresponding to B_2. Another consequence of damping is that the two real solutions of $P(F) = 0$, corresponding to the abscissae of the points B_1 and B_2 in Figure 5b, move farther apart as c increases. Finally, for $c \neq 0$, the roots $\lambda_1(F)$, $\lambda_2(F)$, $\lambda_3(F)$, and $\lambda_4(F)$ are defined analogously to those in Equations* (71a) *and* (71b)*, with $F^{\mathrm{nd}}_{\mathrm{flu}}$ and $F^{\mathrm{nd}}_{\mathrm{div}}$ replaced by $F_{\mathrm{flu}}(c)$ and $F_{\mathrm{div}}(c)$, respectively.*

With reference to Figures 5a and 5b, we now discuss the type of bifurcation occurring in the cases analyzed in Sections 4.1.1 and 4.1.2. In the case without damping, Figure 5a (Section 4.1.1), the double pendulum subsystem becomes a Hamiltonian system and the occurrence of a Hamiltonian Hopf bifurcation is observed [33, 34]. Such a bifurcation occurs when the roots of the characteristic polynomial $Q(\lambda)$ behave as follows (see Figure 6 for a graphical representation of points a., b., and c., below):

a. For $F \in [0, F^{\mathrm{nd}}_{\mathrm{flu}}[$, the four roots of $Q(\lambda)$ are purely imaginary and occur in two complex-conjugate pairs, all distinct from one another. Two of them have strictly positive imaginary part, while the other two have strictly negative imaginary part (see the four distinct curves on the left-hand side of Figure 5a).
b. As the control parameter increases and reaches the critical value $F \equiv F^{\mathrm{nd}}_{\mathrm{flu}}$, the two roots with strictly positive imaginary part coalesce into a single purely imaginary root with positive imaginary part and zero real part. The two roots with strictly negative imaginary part undergo an analogous coalescence, merging into a purely imaginary root with negative imaginary part. The two resulting roots still form a complex-conjugate pair.

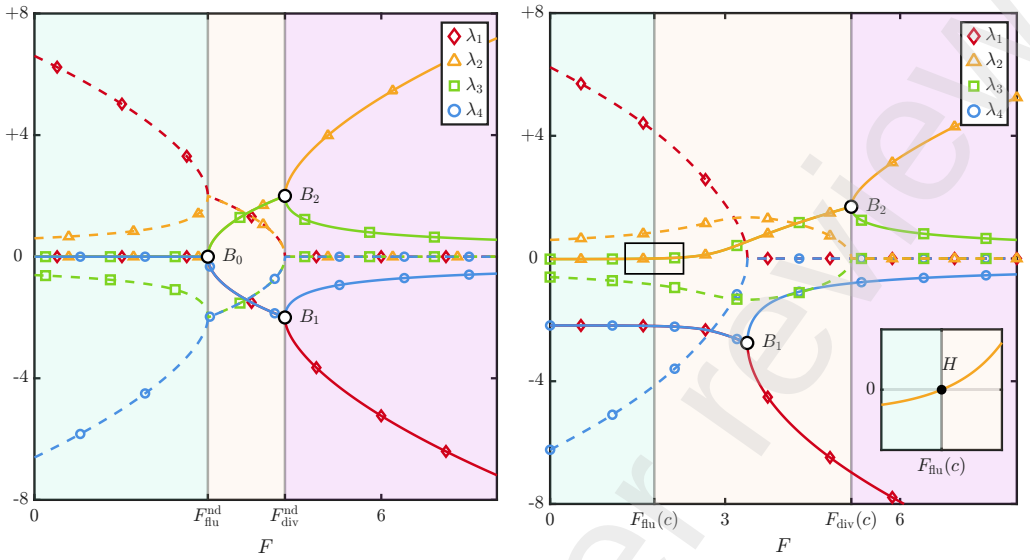

(a) λ-F diagram for the roots of $Q(\lambda)$ in the absence of damping ($c = 0$).

(b) λ-F diagram for the roots of $Q(\lambda)$ in the presence of damping ($c = 0.1$).

Figure 5: Diagrams of the roots of $Q(\lambda)$ in Equation (53) for $c = 0$ and $c = 0.1$.

c. For $F \in]F^{\mathrm{nd}}_{\mathrm{flu}}, F^{\mathrm{nd}}_{\mathrm{div}}[$ (the flutter region), the two coalesced pairs split and acquire nonzero real parts: one with positive real part and the other with negative real part. The corresponding roots are symmetric with respect to the real axis in the λ-F diagram, but they are no longer complex conjugates of one another.

When addressing the case with damping (Figure 5b), a Hopf bifurcation occurs, which will be discussed in detail in the next section.

4.2. Investigation of Hopf bifurcation: from Schur's complement technique to dynamical systems

The Schur's complement technique [20, 27] is used in this section to decouple the computation of the Lagrange multiplier μ from the determination of θ_1, θ_2, and X_{c}. To this end, Equations

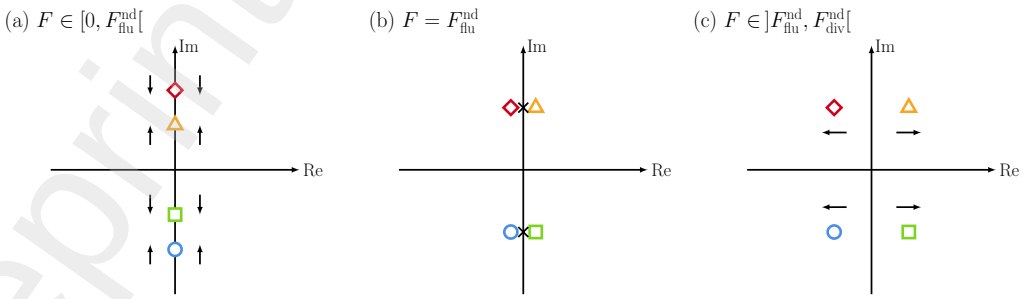

Figure 6: Graphical representation of the behavior of the roots in the case of the Hamiltonian Hopf bifurcation.

(34a)–(34c) and (36) are rewritten in matrix form, isolating the array $\ddot{\mathsf{q}}$ collecting the second-order derivatives $\ddot{q} \equiv (\ddot{\theta}_1, \ddot{\theta}_2, \ddot{X}_\mathrm{c})$ together with the Lagrange multiplier μ. We then reformulate the problem in the *state-variable formalism* and apply dynamical-systems techniques to investigate the stability of the device.

In matrix form, Equations (34a)–(34c) and (36) read

$$\begin{bmatrix} \hat{\mathsf{M}}(\mathsf{q}) & -[\hat{\mathsf{A}}(\mathsf{q})]^{\mathrm{T}} \\ -\hat{\mathsf{A}}(\mathsf{q}) & \mathsf{O} \end{bmatrix} \begin{Bmatrix} \ddot{\mathsf{q}} \\ \mu \end{Bmatrix} = \begin{Bmatrix} \hat{\mathsf{b}}_\mathsf{q}(\mathsf{q}, \dot{\mathsf{q}}, t) \\ \hat{\mathsf{b}}_\mathrm{c}(\mathsf{q}, \dot{\mathsf{q}}) \end{Bmatrix}, \tag{80}$$

where $\hat{\mathsf{M}}(\mathsf{q})$ denotes the 3×3 mass matrix; $\hat{\mathsf{A}}(\mathsf{q})$ is the 1×3 constraint matrix; O is the 1×1 null matrix; $\hat{\mathsf{b}}_\mathsf{q}(\mathsf{q}, \dot{\mathsf{q}}, t)$ is a 3×1 array collecting all the terms appearing in Equations (34a)–(34c) that involve neither the generalized accelerations $\ddot{\theta}_1$, $\ddot{\theta}_2$, and $\ddot{X}_\mathrm{c}$, nor the Lagrange multiplier μ; $\hat{\mathsf{b}}_\mathrm{c}(\mathsf{q}, \dot{\mathsf{q}})$ is the 1×1 array representing the right-hand side of Equation (36). Note that $\hat{\mathsf{b}}_\mathsf{q}(q, \dot{q}, t)$ depends explicitly on time through $B_\mathrm{h}(t)$ and $\dot{B}_\mathrm{h}(t)$. The explicit expressions for $\hat{\mathsf{M}}(\mathsf{q})$, $\hat{\mathsf{A}}(\mathsf{q})$, $\hat{\mathsf{b}}_\mathsf{q}(\mathsf{q}, \dot{\mathsf{q}})$, and $\hat{\mathsf{b}}_\mathrm{c}(\mathsf{q}, \dot{\mathsf{q}})$ are

$$\mathsf{M} \equiv \hat{\mathsf{M}}(\mathsf{q}) \coloneqq \begin{bmatrix} \frac{5}{4} & \frac{1}{2}\cos(\theta_1 - \theta_2) & -\frac{3}{2}\sin\theta_1 \\ \frac{1}{2}\cos(\theta_1 - \theta_2) & \frac{1}{4} & -\frac{1}{2}\sin\theta_2 \\ -\frac{3}{2}\sin\theta_1 & -\frac{1}{2}\sin\theta_2 & M \end{bmatrix}, \tag{81a}$$

$$\mathsf{b}_\mathsf{q} \equiv \hat{\mathsf{b}}_\mathsf{q}(\mathsf{q}, \dot{\mathsf{q}}) \coloneqq \begin{Bmatrix} -\frac{1}{2}\sin(\theta_1 - \theta_2)\,\dot{\theta}_2^2 - c(2\dot{\theta}_1 - \dot{\theta}_2) - (2\theta_1 - \theta_2) \\ \frac{1}{2}\sin(\theta_1 - \theta_2)\dot{\theta}_1^2 - c(\dot{\theta}_2 - \dot{\theta}_1) - (\theta_2 - \theta_1) \\ \frac{3}{2}(\cos\theta_1)\dot{\theta}_1^2 + \frac{1}{2}(\cos\theta_2)\dot{\theta}_2^2 + F \end{Bmatrix} + \begin{Bmatrix} \mathfrak{F}_{\mathrm{L}1} \\ \mathfrak{F}_{\mathrm{L}2} \\ \mathfrak{F}_{\mathrm{L}3} \end{Bmatrix}, \tag{81b}$$

$$\mathsf{b}_\mathrm{c} \equiv \hat{\mathsf{b}}_\mathrm{c}(\mathsf{q}, \dot{\mathsf{q}}) \coloneqq \left\{(\sin\theta_2)\dot{X}_\mathrm{c}\dot{\theta}_2 + \cos(\theta_1 - \theta_2)(\dot{\theta}_1 - \dot{\theta}_2)\dot{\theta}_1\right\}, \tag{81c}$$

$$\mathsf{A} \equiv \hat{\mathsf{A}}(\mathsf{q}) \coloneqq \left[\sin(\theta_1 - \theta_2) \quad 0 \quad -\cos\theta_2\right]. \tag{81d}$$

Since $\hat{\mathsf{M}}(\mathsf{q})$ is an invertible matrix for all values of q, we can apply the Schur complement technique [20, 27, 35] to rewrite system (80) in normal form and, upon introducing the Schur complement $\mathsf{S} \coloneqq \mathsf{A}\mathsf{M}^{-1}\mathsf{A}^{\mathrm{T}}$ of M, we obtain

$$\ddot{\mathsf{q}} = [\mathsf{M}^{-1} - (\mathsf{M}^{-1}\mathsf{A}^{\mathrm{T}})\mathsf{S}^{-1}(\mathsf{A}\mathsf{M}^{-1})]\mathsf{b}_\mathsf{q} - (\mathsf{M}^{-1}\mathsf{A}^{\mathrm{T}})\mathsf{S}^{-1}\mathsf{b}_\mathrm{c}, \tag{82a}$$

$$\mu = -\mathsf{S}^{-1}[(\mathsf{A}\mathsf{M}^{-1})\mathsf{b}_\mathsf{q} + \mathsf{b}_\mathrm{c}]. \tag{82b}$$

Equation (82a) unfolds three scalar equations for the three unknowns collected in q, and, once these are computed, Equation (82b) determines the Lagrange multiplier μ.

A further step beyond Equation (82a) consists in introducing the *state-variable formalism*, which allows us to recast (82a) as a system of six first-order scalar ordinary differential equations. In fact, by setting $Y_1 \coloneqq \theta_1$, $Y_2 \coloneqq \theta_2$, $Y_3 \coloneqq X_\mathrm{c}$, $Y_4 \coloneqq \dot{\theta}_1$, $Y_5 \coloneqq \dot{\theta}_2$, $Y_6 \coloneqq \dot{X}_\mathrm{c}$, and introducing the 6×1 arrays $\mathsf{Y} = \{Y_1 \cdots Y_6\}^{\mathrm{T}}$ and $\dot{\mathsf{Y}} = \{\dot{Y}_1 \cdots \dot{Y}_6\}^{\mathrm{T}}$, Equation (82a) is equivalent to

$$\dot{\mathsf{Y}} = \mathsf{f}(\mathsf{Y}, t; F), \tag{83}$$

where, for $k = 1, 2, 3$, $f_k(\mathsf{Y}, t; F) = Y_{k+3}$, while $f_4(\mathsf{Y}, t; F)$, $f_5(\mathsf{Y}, t; F)$, and $f_6(\mathsf{Y}, t; F)$ are the three components of the right-hand side of Equation (82a), written in the state variable formalism.

In Equation (83), the vector $\mathsf{f}(\mathsf{Y}, t; F)$ inherits its explicit time dependence from $\hat{\mathsf{b}}_\mathsf{q}(\mathsf{q}, \dot{\mathsf{q}}, t)$. However, this dependence appears only in the components $f_4(\mathsf{Y}, t; F)$, $f_5(\mathsf{Y}, t; F)$, and $f_6(\mathsf{Y}, t; F)$.

We also emphasize that we have expressed the functions as parametrically dependent on the dead load F, which plays the role of the bifurcation parameter. Although the characteristic magnetic induction B_{M} may, in principle, influence the stability of the device [5], it is treated here as a fixed parameter for simplicity, and F is taken as the sole bifurcation parameter of the study.

We now investigate the stability of the equilibrium configuration q_{e}, given in Equation (43), following standard dynamical-systems procedures. In particular, we refer to the dynamical system described by Equation (83). Our aim is to assess whether or not the system undergoes a Hopf bifurcation at $F = F_{\mathrm{flu}}(c)$. To this end, we analyze the eigenvalues of the Jacobian matrix of the map f in Equation (83), evaluated at the equilibrium point $\mathsf{Y} = \mathsf{Y}_{\mathrm{e}} = \{0\ 0\ -2\ 0\ 0\ 0\}^{\mathrm{T}}$. This corresponds to expressing q_{e} in the state-variable formalism of Section 4.2, with $X_{\mathrm{ce}} = -2$.

We start considering the first-order Taylor expansion of f at Y_{e} and for a generic value of F. Hence, for $j = 1, \ldots, 6$, and in the limit $\|\mathsf{Y} - \mathsf{Y}_{\mathrm{e}}\|_2 \to 0$, we write

$$[\mathsf{f}(\mathsf{Y}, t; F)]_j = \underbrace{[\mathsf{f}(\mathsf{Y}_{\mathrm{e}}, t; F)]_j}_{=0} + \sum_{k=1}^{6} \underbrace{\left[\frac{\partial f_j}{\partial Y_k}(\mathsf{Y}_{\mathrm{e}}, t; F)\right]}_{=:[\mathsf{J}_{\mathrm{e}}]_{jk}} [Y_k - (Y_{\mathrm{e}})_k] + o(\|\mathsf{Y} - \mathsf{Y}_{\mathrm{e}}\|_2), \tag{84}$$

where $\|\mathsf{p}\|_2 := \sqrt{\mathsf{p}^{\mathrm{T}}\mathsf{p}}$ denotes the 2-norm of a generic (column) array p. The 6×6 Jacobian matrix $\mathsf{J}_{\mathrm{e}} \equiv \hat{\mathsf{J}}(\mathsf{Y}_{\mathrm{e}}, t; F)$ features six eigenvalues given by the roots of the characteristic equation

$$P(\omega; F) = \det(\mathsf{J}_{\mathrm{e}} - \omega \mathsf{I}_6) = \tfrac{1}{M} Q(\omega; F)\, \omega^2 = 0, \tag{85}$$

where $Q(\omega; F)$ is a rewriting of the fourth-grade characteristic polynomial in Equation (53), associated with the double pendulum, with ω replacing λ and the dependence on F made explicit. The roots of $P(\omega; F)$ define the eigenvalues $\omega_1, \ldots, \omega_6$ as functions of F, so that we may write $\omega_j = \hat{\omega}_j(F)$, for $j = 1, \ldots, 6$.

As noticed in Section 4.1 and sketched in Figure 4, the characteristic polynomial $Q(\omega; F)$ remains unchanged regardless of whether or not the Lorentz force is considered, and the same applies to $P(\omega; F)$. Hence, $P(\omega; F)$ and its roots can be used to analyze the occurrence of a Hopf bifurcation as if the Lorentz force were absent, in which case the dynamical system would behave as autonomous.

Although the characteristic equation (85) describes the device as a whole—including the skate, which contributes the factor ω^2 arising from the constraint—the decoupling, in terms of eigenvalues, between the double pendulum and the cart in the linearized analysis of Section 4 is manifested in the factorization shown in Equation (85). Indeed, the characteristic polynomial features two distinct factors: one of grade four for the double pendulum, $Q(\omega; F)$; another of grade two, ω^2, related to the nonholonomic constraint. The presence of the latter can be related to the linearized constraint and, consequently, to the acceleration of the cart $\ddot{x}_{\mathrm{c}}$ in Equation (47d).

When Equation (85) is evaluated at $F = F_{\mathrm{flu}}(c)$, the polynomial $Q(\omega; F)$ becomes

$$Q(\omega; F_{\mathrm{flu}}(c)) = (22 + 44\, c\, \omega + \omega^2)(8/11 + \omega^2) = 0, \tag{86}$$

and the eigenvalues of $\mathsf{J}_{\mathrm{e}} \equiv \hat{\mathsf{J}}(\mathsf{Y}_{\mathrm{e}}, t; F_{\mathrm{flu}}(c))$ are the roots of the characteristic equation

$$P(\omega; F_{\mathrm{flu}}(c)) = \tfrac{1}{M}(22 + 44\, c\, \omega + \omega^2)(8/11 + \omega^2)\omega^2 = 0, \tag{87}$$

which read

$$\underbrace{\omega_{1,2} = -22c \pm \sqrt{-22 + (22c)^2}, \quad \omega_{3,4} = \pm i\sqrt{8/11},}_{\text{double pendulum}} \qquad \underbrace{\omega_{5,6} = 0.}_{\text{constraint}} \tag{88}$$

Moreover, the eigenvalues $\omega_{1,2} \equiv \hat{\omega}_{1,2}(F_{\text{flu}}(c))$ depend parametrically on c both through $F_{\text{flu}}(c)$ and through the coefficients of $Q(\omega; F)$, as shown in Equation (86), although this is not explicitly expressed by the notation used.

The first four roots obtained from Equation (87), ω_1, ω_2, ω_3 and ω_4, are also roots of Equation (86), and refer to the double pendulum, which experiences flutter instability. In particular, the eigenvalues ω_1 and ω_2 are complex conjugate for $c \in]0, 1/\sqrt{22}[$, while they are purely real for $c > 1/\sqrt{22}$, and are coincident for $c = 1/\sqrt{22}$. In all these cases, $\text{Re}[\omega_1]$ and $\text{Re}[\omega_2]$ are negative for all $c > 0$. Hence, ω_1, ω_2, ω_3, and ω_4 characterize the onset of flutter through a Hopf bifurcation [3]. In particular, a Hopf bifurcation at the equilibrium Y_e, occurring at $F \equiv F_{\text{flu}}(c)$, arises if the following three conditions are satisfied [36]:

1. At the onset of flutter, Y_e is an equilibrium state, $\mathsf{f}(\mathsf{Y}_\text{e}, t; F_{\text{flu}}(c)) = \mathsf{0}$;
2. At $F = F_{\text{flu}}(c)$, exactly one pair of purely imaginary complex-conjugate eigenvalues exists, each of algebraic multiplicity one, while all remaining eigenvalues have nonzero real part (in our case, negative real part).
3. The eigenvalues $\omega_3(F)$ and $\omega_4(F) \equiv \bar{\omega}_3(F)$ that, at $F = F_{\text{flu}}(c)$, form to the aforementioned pair of conjugate imaginary eigenvalues must depend on F in such a way that their real part be differentiable at $F_{\text{flu}}(c)$ and compliant with the condition

$$\frac{\mathrm{d}\,\text{Re}[\omega_{3,4}]}{\mathrm{d}F}(F_{\text{flu}}(c)) \neq 0. \tag{89}$$

The fulfillment of these conditions is highlighted in Figure 5b.

Remark 7 (Lorentz force does not affect the onset of the Hopf bifurcation for $F = F_{\text{flu}}(c)$)**.** *It has been shown that, despite the inclusion of the Lorentz force in the model studied by Cazzolli et al. [3], the system still undergoes a Hopf bifurcation under the same conditions, namely when the dead load F reaches the critical flutter load $F_{\text{flu}}(c)$.*

We conclude by noting that a Hopf bifurcation occurs even though the eigenvalues ω_5 and ω_6 vanish and, strictly speaking, do not satisfy the second Hopf condition. Moreover, they make the Jacobian matrix J_e singular and preclude the possibility of computing the first Lyapunov coefficient for the problem as is currently formulated. However, as recalled in Section 4, ω_5 and ω_6 can be disregarded from the study of stability and, thus, of the bifurcations [23]. This argument is grounded in the same reasoning used to derive Equation (52) from Equation (51) in the stability analysis.

5. Post-critical behavior: the Lorentz force influences the flutter instability

In this section, we aim to assess how the Lorentz force can influence the post-critical behavior of the device both in Case I and in Case II.

As anticipated in the preamble of Section 4, we restore the physical dimensions of the problem to provide context for the following numerical test.

5.1. The scenario of a soft bodied microrobot for biological applications

Among the various designs that are often employed in microrobotics [37], we model our microrobot as a continuous rod (discretized by the double pendulum) attached to a small mass (the cart), having both viscous and elastic material properties (the viscoelastic hinges), and a

concentrated electric charge at one end (the point charge $\mathfrak{e}$ in D). Specifically, we assume the rod to be made of an idealized rubber-like material with density $\rho = 10^3\,\mathrm{kg/m^3}$ and Young modulus $E_\mathrm{Y} = 10^6\,\mathrm{Pa}$, [14].

The device's geometry is characterized by slender bars, with length $\ell = 10\,\mu\mathrm{m}$, width $w = 1\,\mu\mathrm{m}$, and thickness $\tau = 0.1\,\mu\mathrm{m}$, so that their volumes and moments of inertia read $V = \ell w \tau$ and $J = (1/12)\tau^3 w$, respectively (the aspect ratio of the bars and the notation are taken from [5]). Consequently, the mass of one bar reads $m = \rho V$, while the stiffness coefficient k is computed as $k = E_\mathrm{Y} J/\ell$ [5]. Once k is obtained, the damping coefficient c (modeling the overall viscous behavior of the robot) is selected coherently with the work by Cazzolli et al. [3]. Hence, c is chosen in such a way that the dimensionless damping coefficient of Equation $(45\mathrm{b})_2$ is $c/(\ell\sqrt{mk}) = 0.1$ (cfr. Section 4).

The value of the dead load F is in line with the typical thrust and propulsion forces reported for microrobots in biological applications [11]. Specifically, we choose the value $F = 1.6\,\mathrm{pN}$, for which flutter can occur, since $F \simeq 1.1\,F_\mathrm{flu}(c)$.

The solenoid is assumed to be sufficiently long, with height at least four times its diameter [17], and radius $R_\mathrm{s} = 5\,\mathrm{cm}$, and capable of generating a magnetic induction field of maximum amplitude $B_\mathrm{M} = 1\,\mathrm{T}$. We emphasize that this value of B_M is higher than those typically used to study, for instance, the motility of micro- or nano-robots in biological environments (usually around the order of magnitude of $10^{-3}\,\mathrm{T}$, [11]). Although the value $B_\mathrm{M} = 1\,\mathrm{T}$ may be considered extreme, we adopt it to make the Lorentz force comparable to the propulsion forces (dead load) considered in [11] and to the follower force. Solenoids with relatively small diameters can nevertheless reach MRI-level magnetic induction fields [38, 39] and can be used for micro-motility applications [40].

The magnetic induction field is assumed to be sinusoidal in time by setting

$$B_\mathrm{h}(t) = B_\mathrm{M}\sin(\Omega\, t), \qquad \text{so that} \qquad \dot{B}_\mathrm{h}(t) = B_\mathrm{M}\Omega\cos(\Omega\, t), \tag{90}$$

with Ω being its frequency of oscillation. In the following sections, we examine the cases $\Omega = 5\,\mathrm{kHz}$ and $\Omega = 10\,\mathrm{kHz}$, consistent with the frequency range adopted by Rousseaux et al. [17] to justify the low-frequency approximation for the vector potential $\boldsymbol{A}$. We restrict the analysis to a parametric study of ω, while all the other parameters are kept fixed.

The point charge concentrated at the skate is in agreement with the effective net charge of micro-metric entities in aqueous media, as documented in electrokinetic studies [12]. We select $\mathfrak{e} = 0.03\,\mathrm{pC}$ rather than the more natural value $\mathfrak{e} = 0.01\,\mathrm{pC}$ to amplify the influence of the Lorentz force, without allowing the magnetic field amplitude to exceed 1 T.

Remark 8 (Implementation details)**.**
The simulations are obtained by numerically solving the Cauchy problem defined by Equation (83)*, together with the array of initial conditions* $\mathsf{Y}_0 = \{0\ 0\ X_{\mathrm{c}0}\ 0\ 0\ 0\}^\mathrm{T}$*. In Case I,* $X_{\mathrm{c}0}$ *is chosen as a small deviation from* X_ce *in Equation* (43)*, while in Case II it is* $X_{\mathrm{c}0} > R_\mathrm{s}$*. Null initial velocities are assumed. Numerical simulations are performed in MATLAB [41] using the adaptive Runge–Kutta (4,5) scheme implemented in the* `ode45` *function for time integration [42].*

5.2. Case I: the Lorentz force triggers flutter and can suppress the horizontal motion

We consider the case in which the device is fully contained within the solenoid and the cart is initially positioned at $X_{\mathrm{c}0} = -1.5\ell$. For this configuration, corresponding to Figure 3b, with $|X_{\mathrm{c}0} - X_\mathrm{ce}| = 0.5\ell$, flutter occurs as induced by the nonzero torque exerted by the electric part

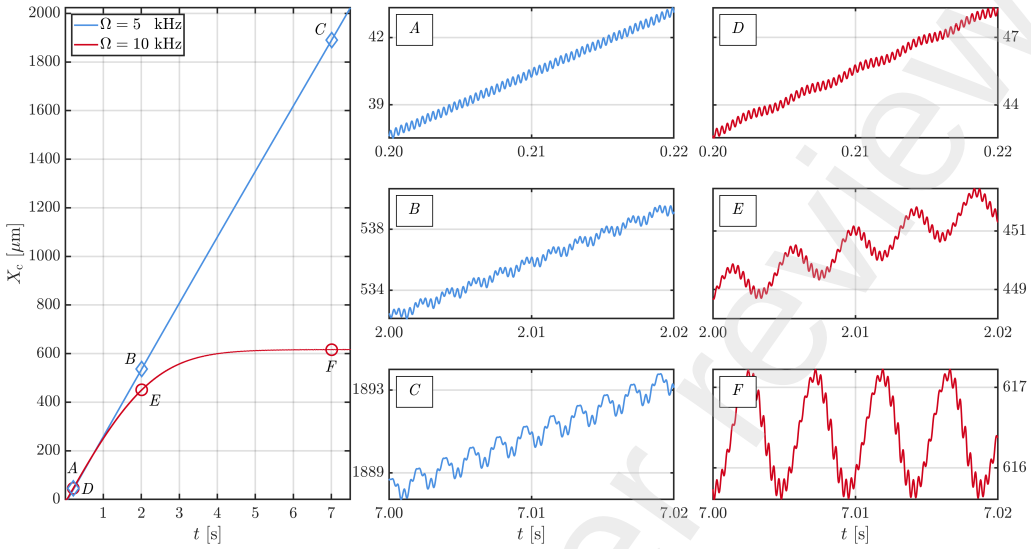

(a) Time trend of X_c for $\Omega = 5$ kHz (blue line with diamonds) and for $\Omega = 10$ kHz (red line with circles).

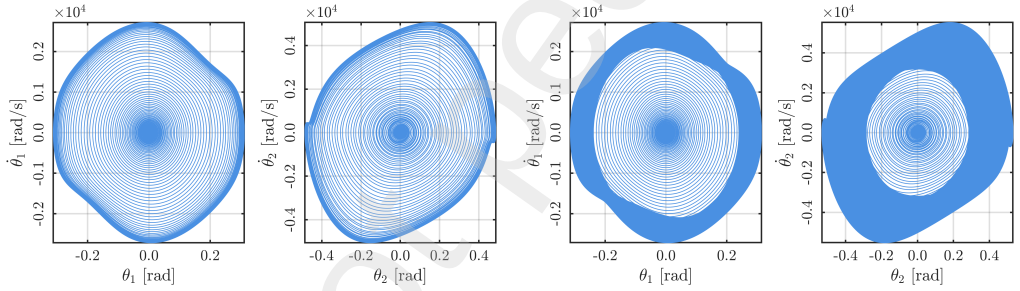

(b) Phase portraits of θ_1 and θ_2, for $\Omega = 5$kHz, over the interval [0 s, 0.1 s], ending with the zoomed-in region A.

(c) Phase portraits of θ_1 and θ_2, for $\Omega = 5$ kHz, over the interval [0 s, 7 s], ending with the zoomed-in region C.

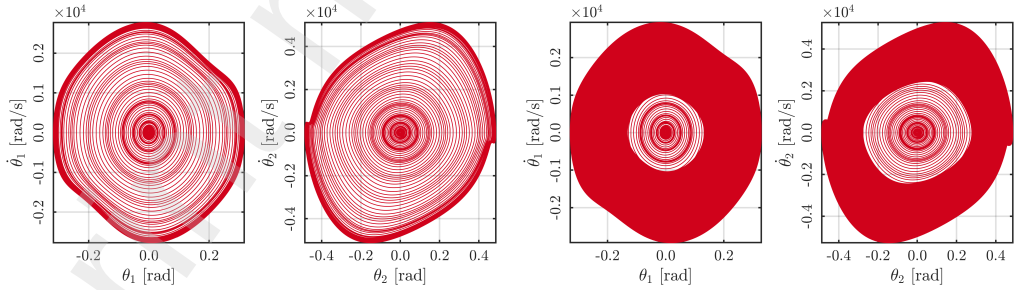

(d) Phase portraits of θ_1 and θ_2, for $\Omega = 10$ kHz, over the interval [0 s, 0.1 s], ending with the zoomed-in region D.

(e) Phase portraits of θ_1 and θ_2, for $\Omega = 10$kHz, over the interval [0 s, 7 s], ending with the zoomed-in region F.

Figure 7: Time trend of X_c and phase portraits of θ_1 and θ_2 concerning the parametric study conducted for Case I and representing the dynamic motion induced by flutter instability on a movable double pendulum with electrically charged nonholonomic constraint and embedded in a magnetic field.

Parameter	Symbol	Value	Unit	Ref.
Length of each bar	ℓ	10	μm	[11, 13]
Mass of each bar	m	0.001	ng	[14]
Mass of the cart	m_c	0.01	ng	–
Spring stiffness	k	10	pC μm	[5]
Damping coefficient	c	0.0001	pN μm s^{-1}	[3]
Dead load	F	1.6	pN	[11]
Electric charge	e	0.03	pC	[12]
Solenoid radius	R_s	5	cm	[38, 39]
Magnetic amplitude	B_M	1	T	[40, 39]
Magnetic frequency	Ω	{5, 10}	kHz	[17]

Table 1: Numerical values used for the simulations.

of the Lorentz force. This phenomenon does not arise in the problem studied by Cazzolli et al. [3], where flutter is triggered only by perturbations of the angles θ_1 or θ_2, or of their associated angular velocities.

We begin with the case $\Omega = 5$ kHz, represented in Figure 7 by the solid blue line marked with diamonds. Figure 7a shows that for $\Omega = 5$ kHz the motion of the cart, described by X_c, exhibits oscillations around a *main, roughly linear, trend*. In spite of the different setting considered in our work, this result is similar to what was found in the paper by Cazzolli et al. [3], in which the cart advances on a large scale with a mean velocity, but it experiences oscillations around such mean velocity on a smaller scale (see the top left panel of Figure 12 of [3]). Regarding the large scale motion, the Lorentz force seems not to affect significantly the dynamics of the cart: the cart moves away from the solenoid center with a comparatively large and approximately constant mean velocity of about $260\,\mu$m s^{-1}, thereby covering about 13 body lengths (2ℓ) per second. However, while the cart's small scale oscillations in our work and in [3] are comparable to each other in the first instants of our simulation (see the zoomed-in region labeled with 'A' in Figure 7a), they are modified by the Lorentz force over time, as the device advances into regions in which the Lorentz force is stronger (see the zoomed-in regions B and C in Figure 7a).

Figures 7b and 7c show the phase portraits of θ_1 and θ_2 for the case $\Omega = 5$ kHz and over the time windows [0 s, 0.1 s] and [0 s, 7 s], respectively. For brevity, the phase portraits corresponding to the intermediate time interval [0 s, 2 s] are not shown.

The increasing amplitude of the oscillations of X_c should be compared with the phase plots of θ_1 and θ_2 in Figures 7b and 7c, and, in particular, with the progressive clustering of the orbits, as time goes by, from Figure 7b (corresponding to the region A) to Figure 7c (corresponding to the region C). Our conclusion is that the Hopf bifurcation, rather than resulting into a stable limit cycle, is characterized by an almost chaotic behavior.

A different situation occurs for $\Omega = 10$ kHz. At this frequency, and with reference to the solid red line marked with circles in Figure 7a, the device no longer experiences a motion similar to that reported by Cazzolli et al. [3]. Indeed, although the cart initially advances as in the case $\Omega = 5$ kHz (and thus as predicted in [3]), exhibiting micro-oscillations in the evolution of X_c (see the zoomed-in regions D, E, and F of Figure 7a), the increasing Lorentz force causes a qualitative change in the motion. The zoomed-in regions D, E, and F in Figure 7a show that X_c oscillates around a *non-linear trend* and that, in this case, the oscillations gain a much more

marked two-scale character with increasing time (from D to F). For $t \geq 7\,\mathrm{s}$, the cart swings in a bounded region of space, without appreciable further advancement, thereby suggesting an average-in-time balance among the dead load, the follower force and the Lorentz force. Also in this case, the oscillations of the cart are to be compared with the progressive thickening of the clusters of orbits reported in Figures 7d and 7e, which show the phase portraits of θ_1 and θ_2 for the case $\Omega = 10\,\mathrm{kHz}$ and over the time windows $[0\,\mathrm{s}, 0.1\,\mathrm{s}]$ and $[0\,\mathrm{s}, 7\,\mathrm{s}]$, respectively. Again, the agglomeration of orbits seems to indicate the tendency of the system towards chaos rather than towards stable limit cycles, with a quasi-periodic behavior.

The increasing impact of the Lorentz force on the flutter instability is also reflected in the phase diagrams of θ_1 and θ_2. Figures 7c and 7e show that the phase portraits of θ_1 and θ_2 do not converge to single closed orbits corresponding to stable limit cycles, in contrast to the behavior reported by Cazzolli et al. [3]. As time progresses, the simulations predict the formation of progressively larger regions, or 'bands', of trajectories in the corresponding phase spaces. This behavior is likely due to the modulations induced by the Lorentz force (Figures 7c and 7e), and is more pronounced in the case with 10 kHz, since the oscillations of the cart around the main trend are stronger than for $\Omega = 5\,\mathrm{kHz}$.

Lastly, we find it worth mentioning that, both for $\Omega = 5\,\mathrm{kHz}$ (region C, corresponding to $t = 7\,\mathrm{s}$) and for $\Omega = 10\,\mathrm{kHz}$ (regions D, E, and F) the Lorentz force seems to induce three-scale dynamics: a main trend, which is linear for $\Omega = 5\,\mathrm{kHz}$ and nonlinear for $\Omega = 10\,\mathrm{kHz}$, 'slow' oscillations, and 'fast' oscillations. The regions C and E of Figure 7a are those in which this phenomenon is best displayed.

5.3. Case II: the Maxwell–Lodge effect in the dynamics of the microrobot

We now consider Case II, in which the device is located outside the solenoid. To characterize its overall motion, we examine the time evolution of the cart position. Owing to the geometric symmetry of the configuration, we analyze two initial placements: one to the left of the solenoid and one to the right, both equidistant from the origin.

Figure 8a illustrates the case in which the cart is positioned to the left of the solenoid. Each of the branches in Figure 8a represents the motion of the cart for different initial conditions X_{c0}, with the upper branch (marked with circles) associated with $X_{c0} = -13.20\,\mathrm{cm}$ and the lower branch (marked with squares) corresponding to $X_{c0} = -13.60\,\mathrm{cm}$. We recall that outside the solenoid any initial position X_{c0} of the cart is of non-equilibrium and therefore Figure 8a shows how the cart evolves, either moving away from the solenoid's boundary (curve marked with circles) or moving towards it (curve marked with squares). Moreover, even if the device is initially in a straight configuration, with $\theta_1(0) = \theta_2(0) = 0$ and $\dot{\theta}_1(0) = \dot{\theta}_2(0) = 0$, the Lorentz force acting on the skate generates an unbalanced torque that induces angular motion of the bars, ultimately leading to flutter, as discussed in Section 4.1. The observed dynamic behavior is argued to be a consequence of the Maxwell–Lodge effect, according to which, even in the absence of the magnetic induction field (see Remark 1 and Equations (16b) and (19b)), the Lorentz force acting on the skate remains nonzero.

In addition, both mean positions of the cart—one with initial position at $-13.20\,\mathrm{cm}$ (circles) and the other at $-13.60\,\mathrm{cm}$ (squares)—tend asymptotically toward a position at approximately $-13.38\,\mathrm{cm}$, about which they oscillate. In view of this behavior, and with a slight abuse of terminology, we refer to the point $(-13.38\,\mathrm{cm}, 0)$ as an 'attractor'. Complementary to the trajectories of the cart X_c converging to the attractor, Figures 8d and 8e also present the phase portraits of the angles θ_1 and θ_2 when the cart is at the attractor, together with a zoomed-in view of the cart

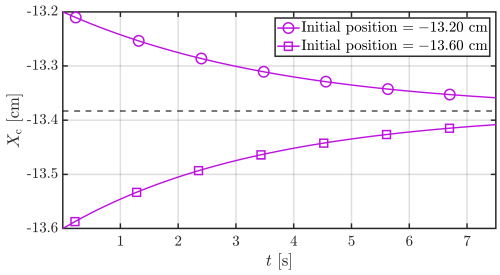

(a) Time trend of X_c, for $\Omega = 10\,\text{kHz}$, when the cart is placed outside of the solenoid on its left, at a position of $-13.20\,\text{cm}$ (circles) and $-13.60\,\text{cm}$ (squares).

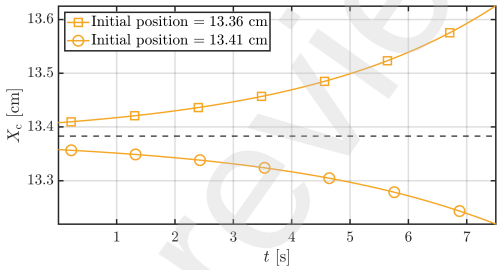

(b) Time trend of X_c, for $\Omega = 10\,\text{kHz}$, when the cart is placed outside of the solenoid on its right, at a position of 13.36 cm (circles) and 13.41 cm (squares).

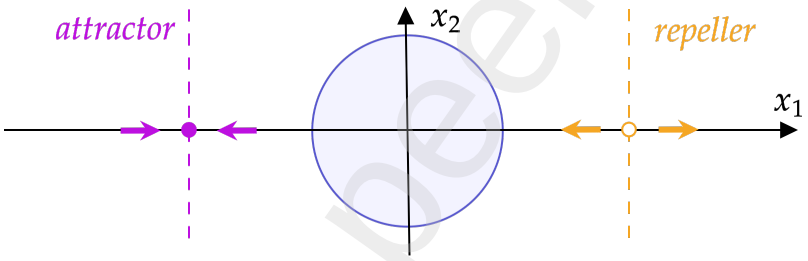

(c) Graphical depiction of the 'attractor' point and 'repeller' point. The picture is not in scale.

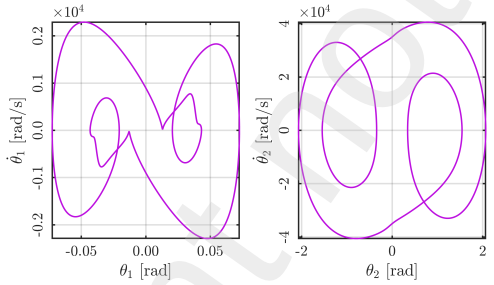

(d) Phase plots of θ_1 and θ_2, at when the device is placed at the point attractor $(-13.38\,\text{cm}, 0)$.

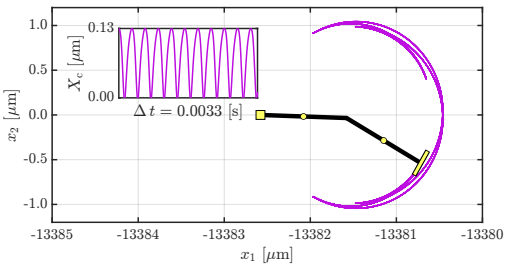

(e) Trace of the position of D alongside the cart oscillations (zoomed in section) at the point attractor $(-13.38\,\text{cm}, 0)$.

Figure 8: Time trend of X_c (a) and (b), picture of the 'attractor' and 'repeller' points (c), phase portraits of θ_1 and θ_2 (d), and trajectory of the point D (e) for the parametric study of Case II and representing the dynamic motion induced by flutter instability on a movable double pendulum with electrically charged nonholonomic constraint, embedded in a magnetic field.

displacement and the trajectory of point D. The dynamical regime in which the device now operates, as observed from the phase portraits, appears to lead to stable limit cycles. This is further illustrated in the zoomed-in view of X_c, where no micro-oscillations are observed to disturb the motion. We believe that, in this case, the Lorentz force acting at the tip of the pendulum is the dominant contribution.

Analogous considerations apply to Figure 8b, although the opposite behavior is observed. For symmetry, we place the cart at two initial positions near the point (13.38 cm, 0), on the right-hand side of the solenoid: $X_{c0} = 13.36\,\text{cm}$ (corresponding to the curve marked with squares) and $X_{c0} = 13.41\,\text{cm}$ (corresponding to the curve marked with circles). The mean trajectories of the cart are now repelled from this point: the one with initial position $X_{c0} = 13.36\,\text{cm}$ moves back toward the solenoid, whereas the one with initial position $X_{c0} = 13.41\,\text{cm}$ moves away from it. Accordingly, we refer to the point $(+13.38\,\text{cm}, 0)$ as a 'repeller'.

Consistent with the discussion above, we emphasize that the device may also undergo backward motion in order to approach the 'attractor' or move away from the 'repeller', as shown in Figure 8. Such behavior is not achievable in the context of the problem studied by Cazzolli et al. [3].

6. Discussion and conclusions

A mechanical structural system has been proposed and analyzed that is capable of generating propulsion from an applied conservative force and a magnetic field by exploiting flutter instability and Hopf bifurcation. The system provides a simple model of a microrobot suitable for operating in magnetically controlled environments, without relying on conventional propulsion mechanisms. Note that, when viscosity is absent, the sole responsible for the variation of energy is the electric part of the Lorentz force. If the latter is switched off, the system becomes indeed conservative.

Our design has coupled a Ziegler double pendulum with a movable cart subject to a dead load and an electrically charged nonholonomic constraint. Electromagnetic interactions provide a Lorentz force applied on the constraint, when placed inside or outside an ideal solenoid. Our setup differs from previously analyzed devices based on electric dipoles or magnetic torques [5].

A primary consequence of the theoretical framework underlying our work is the recognition that the Maxwell–Lodge effect [17, 18] may also be observed in systems such as the microrobot considered here. Owing to the significance of this effect in physics, from both theoretical and experimental perspectives—Rousseaux et al. [17] describe it as the *'classical equivalent'* of the *'Aharonov–Bohm effect [. . .] within quantum physics'*—we found it appropriate to revisit it within our framework (see Remark 1) and to assess its role in the dynamics of the device.

We have proposed two 'virtual' experimental configurations (Case I and Case II), formulated as dedicated Cauchy problems, which may serve as benchmarks for future investigations of the post-critical dynamics of systems similar to ours.

Although the device exhibits behaviors not reported in previous studies, and although the parameters adopted in our simulations are drawn from the literature (see Table 1), the intensity B_M of the magnetic induction field may be relatively high. In particular, we selected $B_M = 1\,\text{T}$—a value achievable in MRI-based and electron-beam experiments [39]—in order to ensure that the Lorentz force is comparable in magnitude to the dead load F typically considered in Ziegler's double pendulum models in microrobotics, as well as to the follower force.

A systematic analysis for smaller values of B_M would be desirable to further delineate the range of validity of the present results. Notwithstanding this limitation, the findings summarized

in Figures 7a–7e and 8a–8b provide a basis for further discussion on the interplay between flutter instability and Hopf bifurcation in devices controlled through additional forces such as the Lorentz force (see Remark 7).

As shown in Figures 8a and 8b, the Lorentz force outside the solenoid—arising solely from the induced electric field—can either attract or repel the microrobot (through its action on the cart), depending on whether the cart is initially positioned below or above a critical distance from the left or right boundary of the solenoid.

The present study contributes to the analysis of the stability of microrobots and related structures inspired by Ziegler's double pendulum, particularly when interactions beyond purely mechanical effects are taken into account. The results may provide a reference framework for future investigations based on alternative experimental configurations and may stimulate the design of new experimental studies in this area.

Authors' contributions

All authors contributed equally to the manuscript.

Declaration of competing interests statement

The authors have no competing interests to declare.

Use of generative Artificial Intelligence (AI)

The authors have *not* used any generative AI tool for writing this work.

References

[1] O. N. Kirillov, Structural optimization of the ziegler's pendulum: singularities and exact optimal solutions, 2010.

[2] D. Bigoni, G. Noselli, Experimental evidence of flutter and divergence instabilities induced by dry friction, Journal of the Mechanics and Physics of Solids 59 (2011) 2208–2226.

[3] A. Cazzolli, F. Dal Corso, D. Bigoni, Non-holonomic constraints inducing flutter instability in structures under conservative loadings, Journal of the Mechanics and Physics of Solids 138 (2020) 103919.

[4] F. D'Annibale, G. Rosi, A. Luongo, Controlling the limit-cycle of the ziegler column via a tuned piezoelectric damper, Mathematical Problems in Engineering 2015 (2015) 1–9.

[5] F. Alouges, A. DeSimone, L. Giraldi, M. Zoppello, Can magnetic multilayers propel artificial microswimmers mimicking sperm cells?, Soft Robotics 2 (2015) 117–128.

[6] H. Ziegler, Principles of Structural Stability, Lehr- und Handbücher der Ingenieurwissenschaften, Birkhäuser Basel, 1977.

[7] X. Wang, C. Fan, S. Yang, Z. Yang, Y. Yang, M. Sinapius, Flutter instability characteristics and mechanisms of ziegler double pendulum with arbitrary masses, stiffness and damping, Nonlinear Dynamics 112 (2024) 20771–20792.

[8] O. Kirillov, F. Verhulst, Paradoxes of dissipation-induced destabilization or who opened whitney's umbrella?, ZAMM - Journal of Applied Mathematics and Mechanics / Zeitschrift für Angewandte Mathematik und Mechanik 90 (2010) 462–488.

[9] O. Kirillov, Nonconservative stability problems of modern physics, volume 14 of *De Gruyter Studies in Mathematical Physics*, 2013.

[10] D. Bigoni, Flutter from Friction in Solids and Structures, 2018.

[11] L. Zhang, K. E. Peyer, B. J. Nelson, Artificial bacterial flagella: Fabrication and magnetic control, Nano Letters 9 (2009) 3663–3667.

[12] A. T. Brown, W. C. K. Poon, Ionic effects in self-propelled pt-coated janus swimmers, Physical Chemistry Chemical Physics 16 (2014) 2446–2458.

[13] H. Shen, S. Cai, Z. Wang, Z. Ge, W. Yang, Magnetically driven microrobots: Recent progress and future development, Materials & Design 227 (2023) 111735.

[14] Y. Kim, G. A. Parada, S. Liu, X. Zhao, Ferromagnetic soft continuum robots, Nature 573 (2019) 82–87.

[15] R. Dreyfus, J. Baudry, M. L. Roper, M. Fermigier, H. A. Stone, J. Bibette, Microscopic artificial swimmers, Nature 437 (2005) 862–865.

[16] F. Katzmeier, F. C. Simmel, Microrobots powered by concentration polarization electrophoresis (cpep), Nature Communications 14 (2023).

[17] G. Rousseaux, R. Kofman, O. Minazzoli, The Maxwell-Lodge effect: significance of electromagnetic potentials in the classical theory, The European Physical Journal D 49 (2008) 249–256.

[18] O. Lodge, On an electrostatic field produced by varying magnetic induction, Proceedings of the Physical Society of London 10 (1889) 116–128.

[19] J. Maruskin, A. Bloch, J. Marsden, D. Zenkov, A fiber bundle approach to the transpositional relations in nonholonomic mechanics, J. Nonlinear Sci. 22 (2012) 431–461.

[20] A. Pastore, A. Giammarini, A. Grillo, Reconciling Kozlov's vakonomic method with the traditional non-holonomic method: solution of two benchmark problems, Acta mechanica (2024).

[21] C. Lanczos, The Variational Principles of Mechanics, Dover Publications, Inc. New York, 1970.

[22] L. A. Pars, A Treatise on Analytical Dynamics, Heinemann, London, 1965.

[23] J. Neimark, N. Fufaev, Dynamics of Nonholonomic Systems, American Mathematical Society, Rhode Island, 1972.

[24] F. Gantmacher, Lectures in Analytical Mechanics, MIR Publishers, Moscow, 1975.

[25] B. Felsager, Geometry, particles, and fields, Springer, Heidelberg, 1998.

[26] K. Haller, Quantum electrodynamics in the temporal gauge, Phys. Rev. D 36 (1987) 1830–1838.

[27] G. Zampieri, Nonholonomic versus vakonomic dynamics, J. Differ. Equ. 163 (2000) 335–347.

[28] A. Agúndez, D. García-Vallejo, E. Freire, Linear stability analysis of nonholonomic multibody systems, International journal of mechanical sciences 198 (2021) 106392.

[29] B. C. Kuo, Automatic Control Systems, 3rd ed., Prentice Hall, 1975.

[30] B. Sturmfels, Solving Systems of Polynomial Equations, Conference Board of the Mathematical Sciences Regional Confe, Conference Board of the Mathematical Sciences, 2002.

[31] J. Sylvester, Xxiii. a method of determining by mere inspection the derivatives from two equations of any degree, The London, Edinburgh, and Dublin Philosophical Magazine and Journal of Science 16 (1840) 132–135.

[32] H. Woody, Polynomial resultants, 2016.

[33] J.-C. van der Meer, The Hamiltonian Hopf Bifurcation, volume 1160 of *Lecture Notes in Mathematics*, Springer-Verlag, Berlin, Heidelberg, 1985.

[34] R. Mazrooei-Sebdani, E. Hakimi, Nondegenerate Hamiltonian Hopf bifurcations in $\omega : 3 : 6$ resonance ($\omega = 1$ or 2), Regular and Chaotic Dynamics 25 (2020) 522–536.

[35] A. Grillo, A. Pastore, S. Di Stefano, An Approach to Growth Mechanics based on the Analytical Mechanics of Nonholonomic Systems, J. Elast. 157 (2025).

[36] Y. A. Kuznetsov, Elements of Applied Bifurcation Theory, volume 112 of *Applied Mathematical Sciences*, 4 ed., Springer Cham, 2023.

[37] R. Xu, Q. Xu, A survey of recent developments in magnetic microrobots for micro-/nanomanipulation, Micromachines 15 (2024) 468.

[38] D. B. Montgomery, Solenoid Magnet Design: The Magnetic and Mechanical Aspects of Resistive and Superconducting Systems, Wiley-Interscience, New York, 1969.

[39] T. Xu, C. J. R. Duncan, P. Denham, B. H. Schaap, A. Kulkarni, D. Garcia, S. D. Anderson, P. Musumeci, R. J. England, Focusing of relativistic electron beams with permanent magnetic solenoid, Phys. Rev. Accel. Beams 28 (2025) 082401.

[40] S. Martel, et al., Mri-based medical nanorobotics: the modulation of magnetic gradients for propulsion and navigation of ferromagnetic core nanocapsules, Applied Physics Letters 90 (2007) 114105.

[41] The MathWorks, Inc., MATLAB, MathWorks, Natick, Massachusetts, 2024. Version R2024b.

[42] L. Shampine, M. Reichelt, The MATLAB ODE Suite, SIAM Journal on Scientific Computing 18 (1997).